

Highlights

An advanced 1D physics-based model for PEM hydrogen fuel cells with enhanced overvoltage prediction

Raphaël Gass, Zhongliang Li, Rachid Outbib, Samir Jemei, Daniel Hissel

- A 1D physics-based PEM fuel cell system model is built for a speed-accuracy trade-off.
- The model is fully described, without intermediary software, for greater flexibility.
- A limiting coefficient s_{lim} is introduced to better model voltage losses.
- The model's static behavior is experimentally validated using polarization curves.
- A discussion on the evolution of simulated internal states is given.

An advanced 1D physics-based model for PEM hydrogen fuel cells with enhanced overvoltage prediction

Raphaël Gass^{a,b,*}, Zhongliang Li^{a,*}, Rachid Outbib^b, Samir Jemei^a, Daniel Hissel^{a,c}

^a*Université de Franche-Comté, UTBM, CNRS, institut FEMTO-ST, FCLAB, Belfort, France*

^b*Aix Marseille Univ, CNRS, LIS, Marseille, France*

^c*Institut Universitaire de France, France*

Abstract

A one-dimensional, dynamic, two-phase, isothermal model of proton exchange membrane fuel cell systems using a finite-difference approach has been developed. This model balances the simplicity of lumped-parameter models with the detailed accuracy of computational fluid dynamics models, offering precise internal state descriptions with low computational demand. The model's static behavior is validated experimentally using polarization curves. In addition, a novel physical parameter, the limit liquid water saturation coefficient (s_{lim}), is introduced in the overvoltage calculation, replacing the traditional limit current density coefficient (i_{lim}). This new parameter links the voltage drop at high current densities to the amount of liquid water present in the catalyst layers and the operating conditions of the fuel cell. Additionally, it has been observed that s_{lim} is influenced at least by the gas pressure applied by the operator. This newly established link is promising for optimizing the control and thereby improving the performance of fuel cells.

Keywords: Proton exchange membrane fuel cell (PEMFC), 1D model, Control-oriented, Limit liquid water saturation coefficient (s_{lim}), Limit current density coefficient (i_{lim}), AlphaPEM

Introduction

To address the environmental consequences of human activities and promote sustainable development, it is imperative to reconsider our current unsustainable energy consumption practices. In this context, hydrogen-based technologies, particularly proton exchange membrane fuel cells (PEMFCs), show potential as a viable alternative to traditional oil usage. However, these technologies face technological obstacles that need to be overcome for large-scale commercialization. For instance, it is necessary to be able to operate PEMFCs at higher power and current densities. To achieve this, the European Union aims to reach 1.2 W.cm^{-2} @ 0.675 V by 2030 [1], while Japan targets 6 kW.l^{-1} and 3.8 A.cm^{-2} for the same year [2]. However, during operation at high current density, PEM fuel cells are prone to experiencing water flooding and oxygen starvation. This susceptibility arises from the rapid electrochemical reactions occurring, leading to performance issues that can be detrimental. One way to manage this is to design models that provide information about the internal states of the stack, where physical sensors cannot be placed. With this information, the diagnostics of PEMFC can be improved, allowing for better dynamic control to enhance the stack performance [3, 4].

Ideally, it would be advisable to always utilize the most accurate PEMFC models that capture the 3D and dynamic characteristics of the stack. These models are considered the most precise available, although the current limits of understanding of fuel cell physics constrains their accuracy. However, these models [5, 6], which rely on commercial software, demand significant computational resources and processing time, making them incompatible with embedded applications. To mitigate this computational burden, partial spatial reductions have been proposed. This involves

*Corresponding authors.

E-mail addresses: raphael.gass@univ-reunion.fr (R. Gass) and zhongliang.li@univ-fcomte.fr (Z. Li)
Website: <https://gassraphael.github.io/>

combining, for example, a 3D model of the gas channels (GC) and gas diffusion layers (GDL) with a 1D model of the catalytic layers (CL) and membrane, forming a so-called "3D+1D" model [7]. Similarly, "2D+1D" models have also been introduced [8, 9]. Other researchers have suggested pseudo-3D ("P3D") models, which, in practice, correspond to multilayered 2D models [10], or simply models exclusively in 2D [11, 12]. Reductive assumptions have also been incorporated, such as stationary, isothermal models with a single phase for water. While these models effectively reduce computational load while maintaining precision in the stack's internal states, they still rely on commercial software and remain too time-consuming for practical use in embedded conditions. They require, for instance, several hours on a high-performance desktop computer to yield results in the case of stationary models. On the other hand, there are highly simplified models that can run quickly on any computer. These are the lumped-parameter models. Among them, the so-called "0D" models physically represent the matter evolution but without modeling the spatial variations within each component. They provide a dynamic view of matter transport as well as a direct representation of the auxiliaries that enable stack control. The foundational work of Pukrushpan et al. [13], whose model is accessible in open-source, has been widely disseminated. However, it is valuable to consider the spatial evolution of the stack's internal states along its thickness because matter variations are significant, and the physical phenomena occurring there are different. To achieve sufficiently precise control of PEMFCs, it seems crucial to retain at least this spatial direction.

To consider the distributed parameters along the stack thickness, 1D, "1D+0D," and "1D+1D" models have been studied. The "1D+0D" [14] and "1D+1D" models [15–19] from the literature are either fast but stationary [14–16] or dynamic but employ numerical solution methods that excessively slow down the model [17–19], rendering them incomplete for dynamic control design in both cases. As for the 1D models [3, 20–25], some are also (partially) stationary [3, 20, 21]. Others incompletely represent matter transports within the MEA [22] or neglect to include the modeling of auxiliaries or bipolar plates [3, 25]. Finally, some models, such as those proposed by Y. Shao et al. and L. Xu et al. [23, 24], are the ones closest to the set objectives: they are fast, dynamic, biphasic, account for the balance of plant and provide sufficiently precise information on all internal states of the stack. However, it is worth noting that their proposed liquid water modeling necessitates the introduction of simplifying assumptions, such as quasi-static equilibrium or an infinite evaporation rate. It is essential to alleviate these assumptions by incorporating insights from alternative 1D models [25] that consider liquid water without resorting to such reductive assumptions. This ensures the credibility of the model predictions.

One objective of the present work is to overcome the drawbacks of the above modelings by developing a comprehensive model of the PEM fuel cell system that eliminates the previous simplifying assumptions regarding the evolution of liquid water, while still maintaining its speed qualities. This model is 1D, dynamic, biphasic, and isothermal. In the developed model, certain involved equations are revised or improved, incorporating findings from recent research and extending upon the authors' prior work [26]. Some original equations have been added and discussed concerning auxiliary variables and voltage calculation to make the model more comprehensive and realistic. In particular, a novel coefficient, named the limit liquid water saturation coefficient (s_{lim}), is introduced to better model the voltage drop at high current densities, establishing a connection between this current density limit and the internal states as well as operating conditions of the cell. Ultimately, this open-source model has been designed to be adopted and extended by other researchers to expedite research in this field. In particular, the coupling of physics-based models like this one with machine learning-based models appears highly promising for producing even faster models while maintaining a very high level of accuracy [27–29].

1. Modeling matter flow in a PEM cell

The model developed in this study is oriented to real-time diagnosis and control purposes. It is therefore needed to take into account both execution speed and accuracy. For instance, regarding the mass transfer process, the model is expected to predict the next tens to hundreds seconds within a few seconds. This enables the controllers to perform multiple model-base predictions within a single control period so that a model predictive control paradigm can be deployed. However, these predictions must also be sufficiently accurate to support the model based diagnosis and control to avoid unintentionally putting the stack in a faulty state or a highly degraded condition, as well as preventing hydrogen waste.

To fulfill these requirements, a one-dimensional (1D) model has been proposed. To achieve efficient gas and water management-related control, real-time access to the dynamically varying spatial distribution of internal states within

the fuel stack is necessary. These states encompass the concentrations of reactants and products, the proportion of liquid or dissolved water in the membrane, and the flow of matter throughout the stack. These variables primarily evolve in the thickness direction of the stack, which is why a 1D model was selected. Furthermore, the condensation of water vapor within the stack is important to consider as flooding must be closely monitored. As a result, the model accounts for two states of water molecules: vapor and liquid, making it a two-phase model. Lastly, it is important to note that the model assumes isothermal conditions and considers that all cell exhibit identical behavior throughout the entire stack. These significant assumptions were made to simplify the complexity of developing the model and are expected to be eliminated in future model versions.

For the model resolution, a finite-difference method is employed to discretize the partial differential equations governed model and transform it into an ordinary differential equations (ODE) governed one. The number and positions of nodes were set appropriately to simplify the model resolution to the utmost extent without losing accuracy. An adaptable numerical method is then applied to solve the transformed ODE.

In the sequel, the finite-difference method, the numerical solution, and the transformed model are presented successively. The balance of plant modeling is discussed in section 2.

1.1. Finite-difference model and its numerical solution

1.1.1. Finite-difference modeling method

Finite-difference modeling involves dividing a system into discrete nodes, with each node representing a specific volume within the system. Within each region, all quantities are assumed to be homogeneous. The value at the center of each volume is then extrapolated to the entire one. Consequently, each node is positioned at the center of its respective region. Therefore, by decreasing the size of the volumes, the simplifying assumption becomes less significant, resulting in a more accurate model.

Within a PEM single cell, there are seven distinct zones. The anode consists of a GDL and a CL. It is in contact with a gas channel (GC) on one side and a membrane on the other side. The configuration is similar on the cathode side, and a single membrane separates the anode from the cathode within the same cell. Each of these zones is composed of different materials or experiences the flow of different molecules. To accurately represent these structures and the matter flow within them, each zone must be assigned a separate node at minimum since each node homogenizes the quantities present within it. Therefore, a minimum of seven nodes is required, corresponding to the seven zones under consideration.

Then, it is also necessary to include an additional node at each GDL, specifically at the boundary with the bipolar plate. These additional nodes are required to account for the material discontinuity between the GDL and the GC, which results in sorption flows between them. Including these nodes accurately captures the sorption flows and ensures the model properly represents this phenomenon.

Furthermore, due to the difference in thickness between the GDL and the CL, it is not enough to only use 9 nodes. Indeed, for the sake of numerical stability, it is advisable to have distances between the nodes of the discretization scheme that are of the same order of magnitude. Ideally, each GDL should have a number of nodes, denoted as n_{gdl} , equal to $\lfloor \frac{H_{gdl}}{H_{cl}} \rfloor$. However, this results in a large number of nodes within the cell, with n_{gdl} generally exceeding 20. Given the number of variables interacting in the GDL, this has a significant computational time cost. In line with the compromise approach of this study, the authors thus propose to take $n_{gdl} = \lfloor \frac{H_{gdl}}{2H_{cl}} \rfloor$.

Finally, figure 1 was generated to illustrate both the overall flows and matter conversions, including their notations, and the placement of model nodes within a PEM single cell.

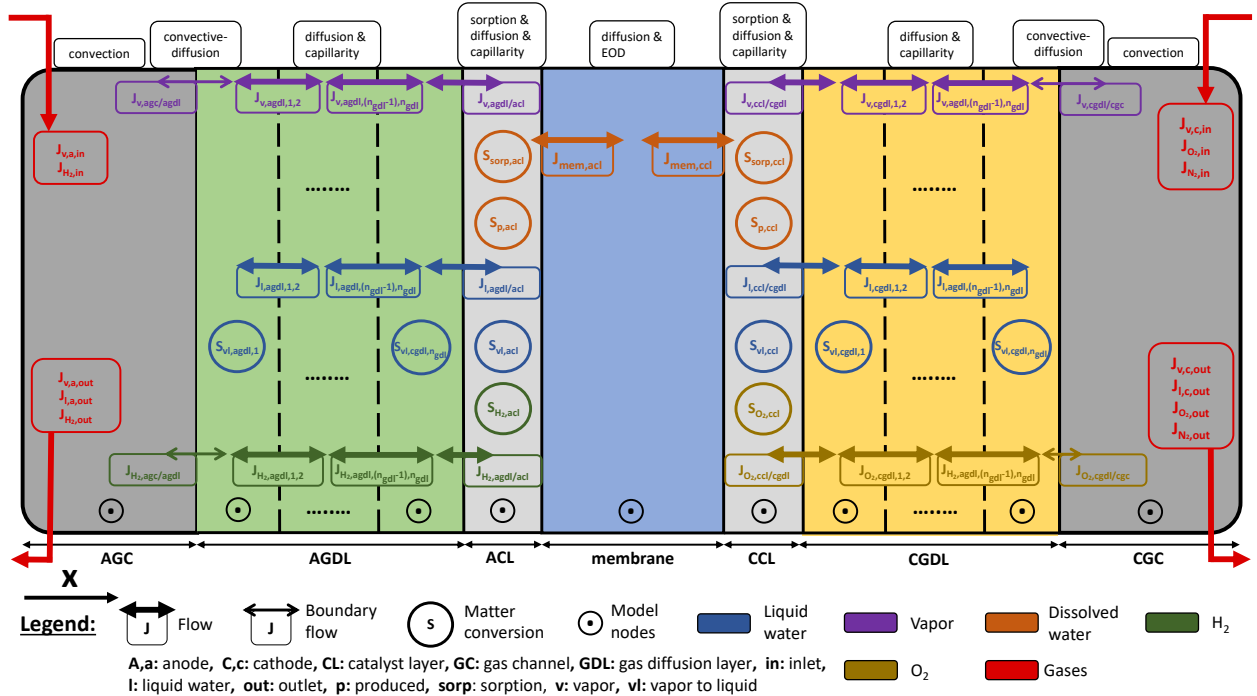


Figure 1: 1D modeling of matter transport phenomena in a PEM single cell divided into several nodes

1.1.2. Numerical solution method

To solve the finite-difference model, the '*BDF*' (Backward Differentiation Formula) method, available in the '*solve_ivp*' function of Python's *scipy.integrate* module, has been utilized [30]. This method offers several advantages.

Firstly, it is an implicit method that guarantees the convergence of results, which is particularly valuable for this model as it involves a stiff problem with high sensitivity to parameters. Indeed, the various physical phenomena in the fuel stack are interconnected. For instance, the consumption of hydrogen leads to the production of dissolved water, which subsequently influences the amount of water vapor or liquid water present. Furthermore, matters evolve at different timescales in the whole fuel cell system. Gases, for example, move much faster compared to liquid water in the stack. This complexity gives rise to a stiff problem that necessitates meticulous numerical solving techniques.

Secondly, this '*BDF*' method employs a non-constant step size, automatically identifying regions of significant changes that require smaller time steps, as well as regions with more gradual changes where larger time steps can be used. This results in a significant reduction in computation time.

Finally, it is important to remember that only methods that can handle stiff problems can be used to solve the proposed model, which excludes most explicit methods.

1.2. The flows and differential equations at stake

1.2.1. Working hypotheses

The assumptions made for the model are listed as follows. The assumptions that were used to develop the mathematical expressions of the flows and differential equations are not mentioned here and are present in the authors' previous work [26].

Overall

- The cells in the concerned stack are identical, in terms of parameters and operating conditions.
- The stack temperature is assumed to be constant and uniform.
- All gas species behave ideally.
- The effect of gravity is ignored.

- Nitrogen concentration is deemed homogeneous across both the cathode and the cathode bipolar plate, with no spatial variation being considered.

In the membrane

- The membrane is considered to be perfectly impermeable to electrons, neglecting the internal short circuit.
- The water generated in the triple point region of the cathode is assumed to be produced in dissolved form in the membrane [31].
- The flow of water through the membrane to a catalytic layer is assumed to be a flow of dissolved water which becomes vapor water [32].
- Since the catalytic layer is very thin compared to the other layers, it is considered that the λ value of the electrolyte present in the CL is instantly the same as at the membrane boundary [24] :

$$\lambda_{acl} = \lim_{x \rightarrow acl} \lambda_{mem} \text{ and } \lambda_{ccl} = \lim_{x \rightarrow ccl} \lambda_{mem}$$

In the GCs

- Liquid water is considered nonexistent in the GC, and a Dirichlet boundary condition [33] is imposed at the GDL/GC interface, setting the liquid water saturation variable s to zero.
- All gases move at the same speed through the GC.
- Water phase change is ignored in the GC.
- All concentrations are uniform in the GC.

1.2.2. Adaptation of mathematical expressions to the finite-difference model

To solve the system of differential equations that describes the matter transports in the stack [26], certain simplifications have been applied to tailor the mathematical expressions to the proposed finite-difference model.

Firstly, the spatial gradients ∇ have been approximated using a partial spatial derivative through the thickness of the cell, denoted as $\frac{\partial}{\partial x} \mathbf{i}$, where \mathbf{i} is a unit vector pointing from the anode to the cathode direction. This simplification is valid because the main circulation of matter occurs along this spatial direction, x . The notation ∂ is retained to indicate that the quantities involved are dependent on other variables, such as time t . Subsequently, this partial derivative $\frac{\partial}{\partial x}$ is replaced by a finite difference between two nodes. These successive simplifications are illustrated in Equation (1), which describes the diffusion of water vapor in the anode:

$$\mathbf{J}_{dif} = -D_v^{eff} \nabla C_v \approx -D_v^{eff} \frac{\partial C_v}{\partial x} \mathbf{i} \approx -2D_v^{eff} \frac{C_{v,acl} - C_{v,agdl,n_gdl}}{H_{gdl}/n_{gdl} + H_{cl}} \mathbf{i} \quad (1)$$

where C_{agdl,n_gdl} is the vapor concentration at the n_{gdl} -th node of the AGDL.

Furthermore, in the calculation of flow between two nodes, many parameters or variables need to be averaged. For instance, in the case of water vapor diffusion mentioned earlier, the effective diffusion coefficient D_v^{eff} is dependent on several factors, including liquid water saturation s , porosity ε , pressure P , and temperature T : $D_v^{eff}(s, \varepsilon, P, T)$. These four quantities, among others, vary spatially. However, when studying the flow between two nodes, it is necessary to assign a single symmetric value for D_v^{eff} . The proposed approach is to average the variables and parameters of two consecutive nodes. Thus, secondary variables and parameters are introduced, as seen in (2) with $s_{agdl,acl}$, $\varepsilon_{agdl,acl}$, $P_{agdl,acl}$ and $T_{agdl,acl}$. In this study, the spatial variation of temperature is implied, although the model assumes an isothermal condition. This is made to facilitate the future implementation of heat transfers.

$$\begin{cases} \mathbf{J}_{dif} = -D_v^{eff}(\mathbf{s}, \varepsilon, P, T) \nabla C_v \approx -2D_v^{eff}(s_{agdl,acl}, \varepsilon_{agdl,acl}, P_{agdl,acl}, T_{agdl,acl}) \frac{C_{v,acl} - C_{v,agdl,n_gdl}}{H_{gdl}/n_{gdl} + H_{cl}} \mathbf{i} \\ s_{agdl,acl} = \frac{s_{agdl,n_gdl} + s_{acl}}{2}, \varepsilon_{agdl,acl} = \frac{\varepsilon_{agdl} + \varepsilon_{acl}}{2}, \\ P_{agdl,acl} = \frac{P_{agdl,n_gdl} + P_{acl}}{2}, T_{agdl,acl} = \frac{T_{agdl,n_gdl} + T_{acl}}{2} \end{cases} \quad (2)$$

1.2.3. Expression of the physical phenomena involved

After incorporating the previously discussed modifications, the differential equations and matter transport expressions outlined in the authors' earlier work [26] can be represented as shown in tables 1 and 2. It should be noted that here the parameter L_{gc} represents the cumulative length of the gas channel, which is the total distance traveled by the gases as they circulate through the bipolar plates. Additionally, the flow coefficients that are functions of internal states have been adjusted for this model and are provided in table 3. Finally, general parameters for modeling the cell are furnished in table 4, while the cell's specific parameters contingent upon the cell type should be identified independently. This will be discussed in Section 4.

Dynamical models	Matter flow expressions
Dissolved water in the membrane	
$\frac{\rho_{mem}\varepsilon_{mc}}{M_{eq}} \frac{d\lambda_{acl}}{dt} = -\frac{J_{\lambda,mem,acl}}{H_{cl}} + S_{sorp,acl} + S_{p,acl}$ $\frac{\rho_{mem}}{M_{eq}} \frac{d\lambda_{mem}}{dt} = \frac{J_{\lambda,mem,acl} - J_{\lambda,mem,ccl}}{H_{mem}}$ $\frac{\rho_{mem}\varepsilon_{mc}}{M_{eq}} \frac{d\lambda_{ccl}}{dt} = \frac{J_{\lambda,mem,ccl}}{H_{cl}} + S_{sorp,ccl} + S_{p,ccl}$	$S_{p,acl} = 2k_{O_2}(\lambda_{mem}, T_{fc}) \frac{RT_{fc}}{H_{cl}H_{mem}} C_{O_2,ccl}$ $S_{sorp,acl} = \gamma_{sorp}(\lambda_{acl}, T_{fc}) \frac{\rho_{mem}}{M_{eq}} [\lambda_{eq}(C_{v,acl}, s_{acl}, T_{fc}) - \lambda_{acl}]$ $J_{\lambda,mem,acl} = \frac{2.5}{22} \frac{i_{fc}}{F} \lambda_{acl,mem} - \frac{2\rho_{mem}}{M_{eq}} D(\lambda_{acl,mem}) \frac{\lambda_{mem} - \lambda_{acl}}{H_{mem} + H_{cl}}$ $J_{\lambda,mem,ccl} = \frac{2.5}{22} \frac{i_{fc}}{F} \lambda_{mem,ccl} - \frac{2\rho_{mem}}{M_{eq}} D(\lambda_{mem,ccl}) \frac{\lambda_{ccl} - \lambda_{mem}}{H_{mem} + H_{cl}}$ $S_{sorp,ccl} = \gamma_{sorp}(\lambda_{ccl}, T_{fc}) \frac{\rho_{mem}}{M_{eq}} [\lambda_{eq}(C_{v,ccl}, s_{ccl}, T_{fc}) - \lambda_{ccl}]$ $S_{p,ccl} = \frac{i_{fc}}{2FH_{cl}} + k_{H_2}(\lambda_{mem}, T_{fc}) \frac{RT}{H_{cl}H_{mem}} C_{H_2,acl}$
Liquid water in the GDL and the CL	
$\forall i \in \llbracket 2, n_{gdl} - 1 \rrbracket :$ $\rho_{H_2O}\varepsilon_{gdl} \frac{d\mathbf{s}_{agdl,i}}{dt} = \frac{J_{l,agdl,(i-1),i} - J_{l,agdl,i,(i+1)}}{H_{gdl}/n_{gdl}} + M_{H_2O}S_{vl,agdl,i}$ $\rho_{H_2O}\varepsilon_{gdl} \frac{d\mathbf{s}_{agdl,n_{gdl}}}{dt} = \frac{J_{l,agdl,(n_{gdl}-1),n_{gdl}} - J_{l,agdl,acl}}{H_{gdl}/n_{gdl}} + M_{H_2O}S_{vl,agdl,n_{gdl}}$ $\rho_{H_2O}\varepsilon_{ccl} \frac{d\mathbf{s}_{acl}}{dt} = \frac{J_{l,agdl,acl}}{H_{cl}} + M_{H_2O}S_{vl,acl}$ $\rho_{H_2O}\varepsilon_{ccl} \frac{d\mathbf{s}_{ccl}}{dt} = \frac{-J_{l,ccl,cgdl}}{H_{cl}} + M_{H_2O}S_{vl,ccl}$ $\rho_{H_2O}\varepsilon_{gdl} \frac{d\mathbf{s}_{cgdl,1}}{dt} = \frac{J_{l,ccl,cgdl} - J_{l,cgdl,1,2}}{H_{gdl}/n_{gdl}} + M_{H_2O}S_{vl,cgdl,1}$ $\rho_{H_2O}\varepsilon_{gdl} \frac{d\mathbf{s}_{cgdl,i}}{dt} = \frac{J_{l,cgdl,(i-1),i} - J_{l,cgdl,i,(i+1)}}{H_{gdl}/n_{gdl}} + M_{H_2O}S_{vl,cgdl,i}$ <p>Boundary conditions: $\mathbf{s}_{agdl,1} = 0, \mathbf{s}_{cgdl,n_{gdl}} = 0$</p>	$\forall i \in \llbracket 1, n_{gdl} - 1 \rrbracket :$ $J_{l,agdl,i,(i+1)} = \sigma(T_{fc}) \frac{K_0(\varepsilon_{gdl})}{\nu_l} \cos(\theta_{c,gdl}) \sqrt{\frac{\varepsilon_{gdl}}{K_0(\varepsilon_{gdl})}} \mathbf{s}_{agdl,i,(i+1)}^e [1.417 - 4.24\mathbf{s}_{agdl,i,(i+1)} + 3.789\mathbf{s}_{agdl,i,(i+1)}^2] \frac{\mathbf{s}_{agdl,(i+1)} - \mathbf{s}_{agdl,i}}{H_{gdl}/n_{gdl}}$ $J_{l,agdl,acl} = 2\sigma(T_{fc}) \frac{K_0(\varepsilon_{gdl,cl})}{\nu_l} \cos(\theta_{c,gdl,cl}) \sqrt{\frac{\varepsilon_{gdl,cl}}{K_0(\varepsilon_{gdl,cl})}} \mathbf{s}_{agdl,acl}^e [1.417 - 4.24\mathbf{s}_{agdl,acl} + 3.789\mathbf{s}_{agdl,acl}^2] \frac{\mathbf{s}_{act} - \mathbf{s}_{agdl,n_{gdl}}}{H_{gdl}/n_{gdl} + H_{cl}}$ $J_{l,ccl,cgdl} = 2\sigma(T_{fc}) \frac{K_0(\varepsilon_{gdl,cl})}{\nu_l} \cos(\theta_{c,gdl,cl}) \sqrt{\frac{\varepsilon_{gdl,cl}}{K_0(\varepsilon_{gdl,cl})}} \mathbf{s}_{ccl,cgdl}^e [1.417 - 4.24\mathbf{s}_{ccl,cgdl} + 3.789\mathbf{s}_{ccl,cgdl}^2] \frac{\mathbf{s}_{ccl,1} - \mathbf{s}_{ccl}}{H_{gdl}/n_{gdl} + H_{cl}}$ $J_{l,cgdl,i,(i+1)} = \sigma(T_{fc}) \frac{K_0(\varepsilon_{gdl})}{\nu_l} \cos(\theta_{c,gdl}) \sqrt{\frac{\varepsilon_{gdl}}{K_0(\varepsilon_{gdl})}} \mathbf{s}_{cgdl,i,(i+1)}^e [1.417 - 4.24\mathbf{s}_{cgdl,i,(i+1)} + 3.789\mathbf{s}_{cgdl,i,(i+1)}^2] \frac{\mathbf{s}_{cgdl,(i+1)} - \mathbf{s}_{cgdl,i}}{H_{gdl}/n_{gdl}}$ $S_{vl} = \begin{cases} \gamma_{cond}\varepsilon(1 - \mathbf{s})x_v(C_v - C_{v,sat}), & \text{if } C_v > C_{v,sat} \\ -\gamma_{evap}\varepsilon\mathbf{s}\frac{\rho_{H_2O}}{M_{H_2O}}RT_{fc}(C_{v,sat} - C_v), & \text{if } C_v \leq C_{v,sat} \end{cases}$
Vapor in the GC	
$\frac{dC_{v,agc}}{dt} = \frac{J_{v,a,in} - J_{v,a,out}}{L_{gc}} - \frac{J_{v,agc,agdl}}{H_{gc}}$ $\frac{dC_{v,cgc}}{dt} = \frac{J_{v,c,in} - J_{v,c,out}}{L_{gc}} + \frac{J_{v,cgdl,cgc}}{H_{gc}}$	$J_{v,a,in} = \frac{\Phi_{asm}P_{sat}(T_{fc})}{P_{asm}} \frac{W_{asm,out}}{H_{gc}W_{gc}M_{asm}}$ $J_{v,a,out} = \frac{\Phi_{agc}P_{sat}(T_{fc})}{P_{agc}} \frac{W_{aem,in}}{H_{gc}W_{gc}M_{agc}}$ $J_{v,c,in} = \frac{\Phi_{csm}P_{sat}(T_{fc})}{P_{csm}} \frac{W_{csm,out}}{H_{gc}W_{gc}M_{csm}}$ $J_{v,c,out} = \frac{\Phi_{cgc}P_{sat}(T_{fc})}{P_{cgc}} \frac{W_{cem,in}}{H_{gc}W_{gc}M_{cgc}}$
Hydrogen and oxygen in the GC	
$\frac{dC_{H_2,agc}}{dt} = \frac{J_{H_2,in} - J_{H_2,out}}{L_{gc}} - \frac{J_{H_2,agc,agdl}}{H_{gc}}$ $\frac{dC_{O_2,cgc}}{dt} = \frac{J_{O_2,in} - J_{O_2,out}}{L_{gc}} + \frac{J_{O_2,cgdl,cgc}}{H_{gc}}$	$J_{H_2,in} = \frac{P_{asm} - \Phi_{asm}P_{sat}(T_{fc})}{P_{asm}} \frac{W_{asm,out}}{H_{gc}W_{gc}M_{asm}}$ $J_{H_2,out} = \frac{P_{agc} - \Phi_{agc}P_{sat}(T_{fc})}{P_{agc}} \frac{W_{aem,in}}{H_{gc}W_{gc}M_{agc}}$ $J_{O_2,in} = y_{O_2,ext} \frac{P_{csm} - \Phi_{csm}P_{sat}(T_{fc})}{P_{csm}} \frac{W_{csm,out}}{H_{gc}W_{gc}M_{csm}}$ $J_{O_2,out} = y_{O_2,cgc} \frac{P_{cgc} - \Phi_{cgc}P_{sat}(T_{fc})}{P_{cgc}} \frac{W_{cem,in}}{H_{gc}W_{gc}M_{cgc}}$
Nitrogen	
$\frac{dC_{N_2}}{dt} = \frac{J_{N_2,in} - J_{N_2,out}}{L_{gc}}$	$J_{N_2,in} = (1 - y_{O_2,ext}) \frac{P_{csm} - \Phi_{csm}P_{sat}(T_{fc})}{P_{csm}} \frac{W_{csm,out}}{H_{gc}W_{gc}M_{csm}}$ $J_{N_2,out} = (1 - y_{O_2,cgc}) \frac{P_{cgc} - \Phi_{cgc}P_{sat}(T_{fc})}{P_{cgc}} \frac{W_{cem,in}}{H_{gc}W_{gc}M_{cgc}}$

Table 1: Synthesis of the differential equations and the associated matter transport expressions in the stack [26] (1/2)

Dynamical models	Matter flow expressions
Vapor in the GDL and the CL	
$\forall i \in \llbracket 2, n_{\text{gdl}} - 1 \rrbracket :$ $\varepsilon_{\text{gdl}} \left[1 - \mathbf{s}_{\text{agdl},1} \right] \frac{dC_{v,\text{agdl},1}}{dt} = \frac{J_{v,\text{agc},\text{agdl}} - J_{v,\text{agdl},1,2}}{H_{\text{gdl}}/n_{\text{gdl}}} - S_{\text{vl},\text{agdl},1}$ $\varepsilon_{\text{gdl}} \left[1 - \mathbf{s}_{\text{agdl},i} \right] \frac{dC_{v,\text{agdl},i}}{dt} = \frac{J_{v,\text{agdl},(i-1),i} - J_{v,\text{agdl},i,(i+1)}}{H_{\text{gdl}}/n_{\text{gdl}}} - S_{\text{vl},\text{agdl},i}$ $\varepsilon_{\text{gdl}} \left[1 - \mathbf{s}_{\text{agdl},n_{\text{gdl}}} \right] \frac{dC_{v,\text{agdl},n_{\text{gdl}}}}{dt} = \frac{J_{v,\text{agdl},(n_{\text{gdl}}-1)} - J_{v,\text{agdl},\text{acl}}}{H_{\text{gdl}}/n_{\text{gdl}}} - S_{\text{vl},\text{agdl},n_{\text{gdl}}}$ $\varepsilon_{\text{cl}} \left[1 - \mathbf{s}_{\text{acl}} \right] \frac{dC_{v,\text{acl}}}{dt} = \frac{J_{v,\text{agdl},\text{acl}}}{H_{\text{cl}}} - S_{\text{sorp},\text{acl}} - S_{\text{vl},\text{acl}}$ $\varepsilon_{\text{cl}} \left[1 - \mathbf{s}_{\text{ccl}} \right] \frac{dC_{v,\text{ccl}}}{dt} = -\frac{J_{v,\text{ccl},\text{cgdl}}}{H_{\text{cl}}} - S_{\text{sorp},\text{ccl}} - S_{\text{vl},\text{ccl}}$ $\varepsilon_{\text{gdl}} \left[1 - \mathbf{s}_{\text{cgdl},1} \right] \frac{dC_{v,\text{cgdl},1}}{dt} = \frac{J_{v,\text{ccl},\text{cgdl}} - J_{v,\text{cgdl},1,2}}{H_{\text{gdl}}/n_{\text{gdl}}} - S_{\text{vl},\text{cgdl},1}$ $\varepsilon_{\text{gdl}} \left[1 - \mathbf{s}_{\text{cgdl},i} \right] \frac{dC_{v,\text{cgdl},i}}{dt} = \frac{J_{v,\text{cgdl},(i-1),i} - J_{v,\text{cgdl},i,(i+1)}}{H_{\text{gdl}}/n_{\text{gdl}}} - S_{\text{vl},\text{cgdl},i}$ $\varepsilon_{\text{gdl}} \left[1 - \mathbf{s}_{\text{cgdl},n_{\text{gdl}}} \right] \frac{dC_{v,\text{cgdl},n_{\text{gdl}}}}{dt} = \frac{J_{v,\text{cgdl},(n_{\text{gdl}}-1)} - J_{v,\text{cgdl},\text{cgc}}}{H_{\text{gdl}}/n_{\text{gdl}}} - S_{\text{vl},\text{cgdl},n_{\text{gdl}}}$	$\forall i \in \llbracket 1, n_{\text{gdl}} - 1 \rrbracket :$ $J_{v,\text{agc},\text{agdl}} = h_a(P_{\text{agc},\text{agdl}}, T_{\text{fc}}) \left[C_{v,\text{agc}} - C_{v,\text{agdl},1} \right]$ $J_{v,\text{agdl},i,(i+1)} = -D_{a,\text{eff}}(\mathbf{s}_{\text{agdl},i,(i+1)}, \varepsilon_{\text{gdl}}, P_{\text{agdl},i,(i+1)}, T_{\text{fc}}) \frac{C_{v,\text{agdl},(i+1)} - C_{v,\text{agdl},i}}{H_{\text{gdl}}/n_{\text{gdl}}}$ $J_{v,\text{agdl},\text{acl}} = -2D_{a,\text{eff}}(\mathbf{s}_{\text{agdl},\text{acl}}, \varepsilon_{\text{agdl},\text{acl}}, P_{\text{agdl},\text{acl}}, T_{\text{fc}}) \frac{C_{v,\text{act}} - C_{v,\text{agdl},n_{\text{gdl}}}}{H_{\text{gdl}}/n_{\text{gdl}} + H_{\text{cl}}}$ $J_{v,\text{ccl},\text{cgdl}} = -2D_{c,\text{eff}}(\mathbf{s}_{\text{ccl},\text{cgdl}}, \varepsilon_{\text{ccl},\text{cgdl}}, P_{\text{ccl},\text{cgdl}}, T_{\text{fc}}) \frac{C_{v,\text{cgdl},1} - C_{v,\text{ccl}}}{H_{\text{gdl}}/n_{\text{gdl}} + H_{\text{cl}}}$ $J_{v,\text{cgdl},i,(i+1)} = -D_{c,\text{eff}}(\mathbf{s}_{\text{cgdl},i,(i+1)}, \varepsilon_{\text{gdl}}, P_{\text{cgdl},i,(i+1)}, T_{\text{fc}}) \frac{C_{v,\text{cgdl},(i+1)} - C_{v,\text{cgdl},i}}{H_{\text{gdl}}/n_{\text{gdl}}}$ $J_{v,\text{cgdl},\text{cgc}} = h_c(P_{\text{cgdl},\text{cgc}}, T_{\text{fc}}) \left[C_{v,\text{cgdl},n_{\text{cgdl}}} - C_{v,\text{cgc}} \right]$
Hydrogen in the GDL and the CL	
$\forall i \in \llbracket 2, n_{\text{gdl}} - 1 \rrbracket :$ $\varepsilon_{\text{gdl}} \left[1 - \mathbf{s}_{\text{agdl},1} \right] \frac{dC_{H_2,\text{agdl},1}}{dt} = \frac{J_{H_2,\text{agc},\text{agdl}} - J_{H_2,\text{agdl},1,2}}{H_{\text{gdl}}/n_{\text{gdl}}}$ $\varepsilon_{\text{gdl}} \left[1 - \mathbf{s}_{\text{agdl},i} \right] \frac{dC_{H_2,\text{agdl},i}}{dt} = \frac{J_{H_2,\text{agdl},(i-1),i} - J_{H_2,\text{agdl},i,(i+1)}}{H_{\text{gdl}}/n_{\text{gdl}}}$ $\varepsilon_{\text{gdl}} \left[1 - \mathbf{s}_{\text{agdl},n_{\text{gdl}}} \right] \frac{dC_{H_2,\text{agdl},n_{\text{gdl}}}}{dt} = \frac{J_{H_2,\text{agdl},(n_{\text{gdl}}-1)} - J_{H_2,\text{agdl},\text{acl}}}{H_{\text{gdl}}/n_{\text{gdl}}}$ $\varepsilon_{\text{cl}} \left[1 - \mathbf{s}_{\text{acl}} \right] \frac{dC_{H_2,\text{acl}}}{dt} = \frac{J_{H_2,\text{agdl},\text{acl}}}{H_{\text{cl}}} + S_{H_2,\text{acl}}$	$\forall i \in \llbracket 1, n_{\text{gdl}} - 1 \rrbracket :$ $J_{H_2,\text{agc},\text{agdl}} = h_a(P_{\text{agc},\text{agdl}}, T_{\text{fc}}) \left[C_{H_2,\text{agc}} - C_{H_2,\text{agdl},1} \right]$ $J_{H_2,\text{agdl},i,(i+1)} = -D_{a,\text{eff}}(\mathbf{s}_{\text{agdl},i,(i+1)}, \varepsilon_{\text{gdl}}, P_{\text{agdl},i,(i+1)}, T_{\text{fc}}) \frac{C_{H_2,\text{agdl},(i+1)} - C_{H_2,\text{agdl},i}}{H_{\text{gdl}}/n_{\text{gdl}}}$ $J_{H_2,\text{agdl},\text{acl}} = -2D_{a,\text{eff}}(\mathbf{s}_{\text{agdl},\text{acl}}, \varepsilon_{\text{agdl},\text{acl}}, P_{\text{agdl},\text{acl}}, T_{\text{fc}}) \frac{C_{H_2,\text{act}} - C_{H_2,\text{agdl},n_{\text{gdl}}}}{H_{\text{gdl}}/n_{\text{gdl}} + H_{\text{cl}}}$ $S_{H_2,\text{acl}} = -\frac{i_{\text{fc}}}{2FH_{\text{cl}}} - \frac{RT_{\text{fc}}}{H_{\text{cl}}H_{\text{mem}}} \left[k_{H_2}(\lambda_{\text{mem}}, T_{\text{fc}}) C_{H_2,\text{acl}} + 2k_{O_2}(\lambda_{\text{mem}}, T_{\text{fc}}) C_{O_2,\text{ccl}} \right]$
Oxygen in the GDL and the CL	
$\forall i \in \llbracket 2, n_{\text{gdl}} - 1 \rrbracket :$ $\varepsilon_{\text{cl}} \left[1 - \mathbf{s}_{\text{ccl}} \right] \frac{dC_{O_2,\text{ccl}}}{dt} = \frac{-J_{O_2,\text{ccl},\text{cgdl}}}{H_{\text{cl}}} + S_{O_2,\text{ccl}}$ $\varepsilon_{\text{gdl}} \left[1 - \mathbf{s}_{\text{cgdl},1} \right] \frac{dC_{O_2,\text{cgdl},1}}{dt} = \frac{J_{O_2,\text{ccl},\text{cgdl}} - J_{O_2,\text{cgdl},1,2}}{H_{\text{gdl}}/n_{\text{gdl}}}$ $\varepsilon_{\text{gdl}} \left[1 - \mathbf{s}_{\text{cgdl},i} \right] \frac{dC_{O_2,\text{cgdl},i}}{dt} = \frac{J_{O_2,\text{cgdl},(i-1),i} - J_{O_2,\text{cgdl},i,(i+1)}}{H_{\text{gdl}}/n_{\text{gdl}}}$ $\varepsilon_{\text{gdl}} \left[1 - \mathbf{s}_{\text{cgdl},n_{\text{gdl}}} \right] \frac{dC_{O_2,\text{cgdl},n_{\text{gdl}}}}{dt} = \frac{J_{O_2,\text{cgdl},(n_{\text{gdl}}-1)} - J_{O_2,\text{cgdl},\text{cgc}}}{H_{\text{gdl}}/n_{\text{gdl}}}$	$\forall i \in \llbracket 1, n_{\text{gdl}} - 1 \rrbracket :$ $S_{O_2,\text{ccl}} = -\frac{i_{\text{fc}}}{4FH_{\text{cl}}} - \frac{RT_{\text{fc}}}{H_{\text{cl}}H_{\text{mem}}} \left[k_{O_2}(\lambda_{\text{mem}}, T_{\text{fc}}) C_{O_2,\text{ccl}} + \frac{k_{H_2}(\lambda_{\text{mem}}, T_{\text{fc}})}{2} C_{H_2,\text{acl}} \right]$ $J_{O_2,\text{ccl},\text{cgdl}} = -2D_{c,\text{eff}}(\mathbf{s}_{\text{ccl},\text{cgdl}}, \varepsilon_{\text{ccl},\text{cgdl}}, P_{\text{ccl},\text{cgdl}}, T_{\text{fc}}) \frac{C_{O_2,\text{cgdl},1} - C_{O_2,\text{ccl}}}{H_{\text{gdl}}/n_{\text{gdl}} + H_{\text{cl}}}$ $J_{O_2,\text{cgdl},i,(i+1)} = -D_{c,\text{eff}}(\mathbf{s}_{\text{cgdl},i,(i+1)}, \varepsilon_{\text{gdl}}, P_{\text{cgdl},i,(i+1)}, T_{\text{fc}}) \frac{C_{O_2,\text{cgdl},(i+1)} - C_{O_2,\text{cgdl},i}}{H_{\text{gdl}}/n_{\text{gdl}}}$ $J_{O_2,\text{cgdl},\text{cgc}} = h_c(P_{\text{cgdl},\text{cgc}}, T_{\text{fc}}) \left[C_{O_2,\text{cgdl},n_{\text{cgdl}}} - C_{O_2,\text{cgc}} \right]$

Table 2: Synthesis of the differential equations and the associated matter transport expressions in the stack [26] (2/2)

Coefficients associated to the dissolved water in the membrane		
$a_w(C_v, s) = \frac{C_v}{C_{v,sat}} + 2s$	(3)	$D(\lambda) = 4.1 \times 10^{-10} \left[\frac{\lambda}{25.0} \right]^{0.15} \left[1.0 + \tanh \left(\frac{\lambda - 2.5}{1.4} \right) \right]$
$\lambda_{eq}^{cl} = \frac{1}{2} (0.300 + 10.8a_w - 16.0a_w^2 + 14.1a_w^3) \cdot (1 - \tanh [100(a_w - 1)]) + \frac{1}{2} (9.2 + 8.6 (1 - \exp [-K_{shape}(a_w - 1)])) \cdot (1 + \tanh [100(a_w - 1)])$		(5)
$f_v(\lambda) = \frac{\lambda V_w}{V_{mem} + \lambda V_w}$	(6)	$\gamma_{sorp}(\lambda, T_{fc}) = \begin{cases} \frac{1.14 \cdot 10^{-5} f_v(\lambda)}{H_{cl}} e^{2416 \left[\frac{1}{303} - \frac{1}{T_{fc}} \right]}, & \text{absorption flow} \\ \frac{4.59 \cdot 10^{-5} f_v(\lambda)}{H_{cl}} e^{2416 \left[\frac{1}{303} - \frac{1}{T_{fc}} \right]}, & \text{desorption flow} \end{cases}$
Coefficients associated to liquid water in the GDL and the CL		
$K_0(\varepsilon) = \frac{\varepsilon}{8 \ln(\varepsilon)^2} \frac{[\varepsilon - \varepsilon_p]^{\alpha+2} r_f^2}{[1 - \varepsilon_p]^{\alpha} [\alpha + 1] \varepsilon - \varepsilon_p^2} e^{\beta_1 \varepsilon_c}$	(8)	$\sigma(T_{fc}) = 235.8 \times 10^{-3} \left[\frac{647.15 - T_{fc}}{647.15} \right]^{1.256} \left[1 - 0.625 \frac{647.15 - T_{fc}}{647.15} \right]$
Coefficients associated to vapor inside the GDL and the CL		
$\begin{cases} D_{a,eff}(s, \varepsilon, P, T_{fc}) = \varepsilon^{\left[\frac{\varepsilon - \varepsilon_p}{1 - \varepsilon_p} \right]^\alpha} [1 - s]^2 e^{\beta_2 \varepsilon_c} D_a(P, T_{fc}) \\ D_{c,eff}(s, \varepsilon, P, T_{fc}) = \varepsilon^{\left[\frac{\varepsilon - \varepsilon_p}{1 - \varepsilon_p} \right]^\alpha} [1 - s]^2 e^{\beta_2 \varepsilon_c} D_c(P, T_{fc}) \end{cases}$	(10)	$\begin{cases} D_a(P, T_{fc}) = 1.644 \cdot 10^{-4} \left[\frac{T_{fc}}{333} \right]^{2.334} \left[\frac{101325}{P} \right] \\ D_c(P, T_{fc}) = 3.242 \cdot 10^{-5} \left[\frac{T_{fc}}{333} \right]^{2.334} \left[\frac{101325}{P} \right] \end{cases}$
$h_i(P, T_{fc}) = S_h \frac{D_i(P, T_{fc})}{H_{gc}}$ $\forall i \in \{a, c\}$	(12)	$S_h = 0.9247 \cdot \ln \left(\frac{W_{gc}}{H_{gc}} \right) + 2.3787$
Coefficients associated to H_2 and O_2 in the CL		
$k_{H_2}(\lambda, T_{fc}) = \begin{cases} \kappa_{co} [0.29 + 2.2 f_v(\lambda)] 10^{-14} \exp \left(\frac{E_{act,H_2,v}}{R} \left[\frac{1}{T_{ref}} - \frac{1}{T_{fc}} \right] \right) & \text{if } \lambda < 17.6 \\ \kappa_{co} 1.8 \cdot 10^{-14} \exp \left(\frac{E_{act,H_2,l}}{R} \left[\frac{1}{T_{ref}} - \frac{1}{T_{fc}} \right] \right) & \text{if } \lambda \geq 17.6 \end{cases}$		(14)
$k_{O_2}(\lambda, T_{fc}) = \begin{cases} \kappa_{co} [0.11 + 1.9 f_v(\lambda)] 10^{-14} \exp \left(\frac{E_{act,O_2,v}}{R} \left[\frac{1}{T_{ref}} - \frac{1}{T_{fc}} \right] \right) & \text{if } \lambda < 17.6 \\ \kappa_{co} 1.2 \cdot 10^{-14} \exp \left(\frac{E_{act,O_2,l}}{R} \left[\frac{1}{T_{ref}} - \frac{1}{T_{fc}} \right] \right) & \text{if } \lambda \geq 17.6 \end{cases}$		(15)

Table 3: Synthesis of the flow coefficients [26]

Symbol	Name (Unit)	Value
Cell model parameters		
ρ_{mem}	Density of the dry membrane ($kg.m^{-3}$)	1980
M_{eq}	Equivalent molar mass of ionomer ($kg.mol^{-1}$)	1.1
ε_{cl}	Porosity of the catalyst layer	0.25
$\theta_{c,gdl}$	Contact angle of GDL for liquid water (rad)	$\frac{2}{3}\pi$ (120°)
$\theta_{c,cl}$	Contact angle of CL for liquid water (rad)	1.66 (95°)
γ_{cond}	Overall condensation rate constant for water (s^{-1})	$5 \cdot 10^3$
γ_{evap}	Overall evaporation rate constant for water ($Pa^{-1}.s^{-1}$)	10^{-4}
K_{shape}	Mathematical factor governing λ_{eq} smoothing	2
Physical constants		
F	Faraday constant ($C.mol^{-1}$)	96485
R	Universal gas constant ($J.mol^{-1}.K^{-1}$)	8.314

Table 4: Synthesis of the general parameters for the cell modeling [26]

2. Balance of plant modeling of a PEMFC system

2.1. An anodic recirculation PEMFC system

In this study, the focus was on considering a fuel cell system rather than examining a single cell only. This approach enables the observation of the auxiliary components' impact on the fuel cells' internal states and performance, which is crucial for control design. Within this investigation, a conventional fuel cell system for vehicles is studied and depicted in figure 2. Specifically, on the anode side, there is a hydrogen storage tank where H_2 is maintained at a desired temperature T . It is connected to a pressure relief valve that delivers pure H_2 to the supply manifold of the anodic chamber. At the outlet of this chamber, there is an exhaust manifold connected both to an electronic purge valve and to a pump that recirculates H_2 back to the supply anode manifold. On the cathode side, a compressor supplies ambient air to the stack, passing successively through a heat exchanger, a humidifier, and a supply cathode manifold. At the outlet of the cathodic chamber, an exhaust manifold is directly linked to an electronic back pressure valve. Finally, this valve releases the gases into the atmosphere, without recovering heat or water from the exhaust air.

Thus, with this setup, the fuel cell can be controlled by the user. On the anode side, the inlet pressure is regulated by the pressure relief valve, and the inlet flow by the recirculation pump. It is also assumed here that the hydrogen within its reservoir is maintained at the desired temperature. On the cathode side, the temperature and humidity of the incoming gases are controlled through the heat exchanger and the humidifier. The compressor dictates an inlet flow, and the back-pressure valve regulates the pressure within the cell.

Remark: This configuration is a simplified version of the one predominantly employed in embedded applications. Yet, during the model validation phase, a modified anode gas supply configuration, similar to the cathode, is utilized to have more flexible control over the operating conditions. This approach is frequently employed in laboratory settings.

2.2. A 0D, dynamic and isothermal model of the auxiliary system

For this study, the aim is not to extensively model the auxiliary system. A simple approach is proposed, based on the foundational work of Pukrushpan et al. [13] and in line with the works of Liangfei Xu et al. [22], Y. Shao et al. [23] and Ling Xu et al. [24]. These works already provide a clear explanation of the auxiliaries' modeling, and readers are encouraged to refer to them for a more detailed understanding. In the present article, the equations derived from these works are directly adopted, with some additions and modifications detailed below. It is worth noting that the mathematical quantity describing the material flows in auxiliaries is traditionally denoted as W and is in $kg.s^{-1}$, unlike the flows in the cells which are traditionally denoted as J , are calculated per area, and primarily molar ($mol.m^{-2}.s^{-1}$).

Several simplifying assumptions have been considered here for the modeling of this auxiliary system:

- Each of the mentioned components is modeled in 0D, meaning the internal parameters in each component are homogeneous.
- The current model is isothermal, implying that the temperature T_{fc} is assumed constant throughout the fuel cell system. Thus, the heat exchanger is disregarded here. This assumption is significant, but is expected to be eliminated in future works.

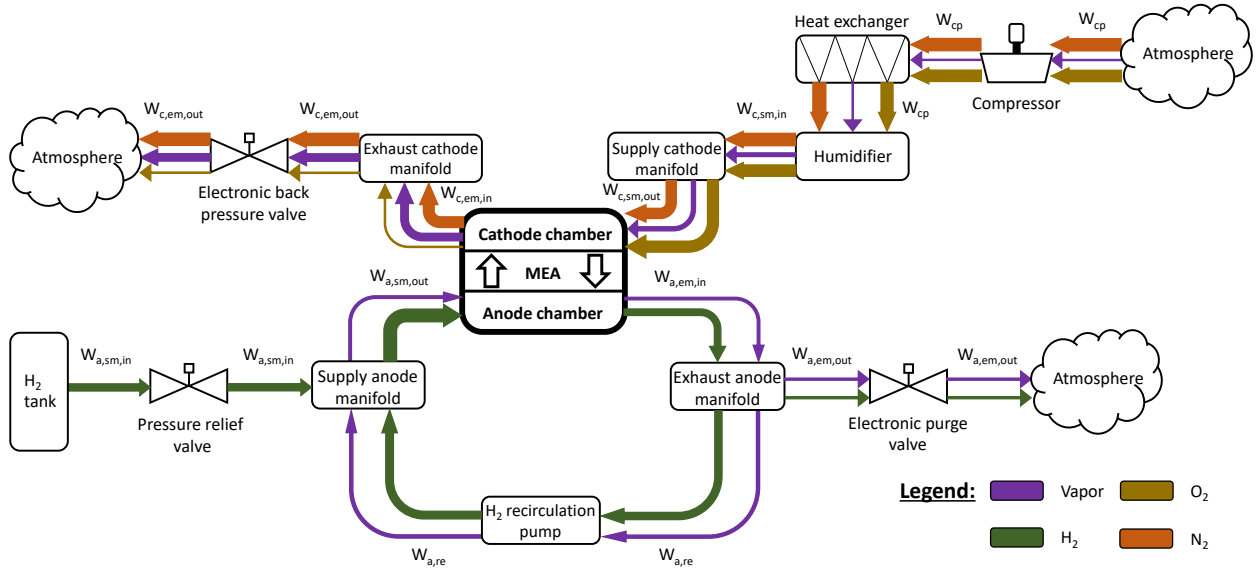


Figure 2: The studied simplified structure of a PEMFC system, consisting of a forced-convective cathode and anodic recirculation.

- Pressure losses along fuel cell gas channels are not modeled.
- The liquid water separator is not modeled. It is assumed that water droplets evacuate so rapidly and efficiently that they do not exist in the auxiliaries. Similarly, any condensation within the auxiliary components is presumed to be promptly removed.
- The H_2 tank and its pressure relief valve are not directly modeled. It is assumed that this reservoir is infinite, and its valve is perfectly regulated to continuously produce a flow at a constant controlled pressure $P_{a,des}$ at the inlet of the supply anode manifold.
- The electronic purge valve is inactive in this study and so $k_{purge} = 0$ in (30).
- The dynamic behavior of the compressor and humidifier is simplified at first order considering the desired steady-state flows $W_{cp,des}$ and $W_{c,inj,des}$, along with the time constants τ_{cp} and τ_{hum} .
- It is assumed that the pressure at the compressor outlet equals the pressure in the supply manifold of the cathode: $P_{cp} = P_{csm}$.
- It is considered that the recirculation pump reaches its steady state instantly, being much faster than other devices.

Certain additions have also been made compared to the existing auxiliary models, such as calculating the humidities in the manifolds (following the same principles stated by Pukrushpan et al. [13]) and controlling the back pressure valve to set the pressure in the stack. The cathode back pressure valve is modeled using a proportional derivative controller as shown in (46). This is an original idea presented in this paper. The throttle area of this valve, denoted as $A_{bp,c}$, with $A_{bp,c} \in [0, A_T]$, is controlled to affect the quantity of matter exiting the cell and thereby influencing the upstream pressure, P_{cgc} here. Then, the proportionality constant K_p is set by considering that the valve takes two seconds to fully open or close and that, during this period, the pressure can change by 0.1 bar. The derivative constant K_d is obtained empirically.

The linearization of several flows is employed in (22), (25), (28), (36) and (38). The exhaust manifolds outflows, in (30) and (40), are not linearized because the pressure difference between the interior of the fuel cell system and the external environment can be significant. Additionally, it has been assumed here that the outflow is necessarily subcritical to avoid the additional instability associated with the piecewise-defined function proposed by Pukrushpan

et al. [13]. Furthermore, it should be noted that there are persistent errors in the literature regarding these equations, specifically the omission of the molar mass under the square root and the confusion between sonic and supersonic flows [13, 22, 24]. Finally, in these equations, γ_{H_2} and γ_a are considered constants, their value changing only slightly with the alteration of flow composition.

Knowing these hypotheses and based on the previously mentioned works [13, 22–24], it is possible to construct the system of differential equations, presented in table 7, which describes the studied auxiliary system. Additionally, the molar masses equations and the balance of plant parameters are provided in tables 5 and 6.

Molar masses equations	
$M_{asm} = \frac{\Phi_{asm} P_{sat}(T_{fc})}{P_{asm}} M_{H_2O} + \frac{P_{asm} - \Phi_{asm} P_{sat}(T_{fc})}{P_{asm}} M_{H_2}$	(16)
$M_{aem} = \frac{\Phi_{aem} P_{sat}(T_{fc})}{P_{aem}} M_{H_2O} + \frac{P_{aem} - \Phi_{aem} P_{sat}(T_{fc})}{P_{aem}} M_{H_2}$	(17)
$M_{csm} = \frac{\Phi_{csm} P_{sat}(T_{fc})}{P_{csm}} M_{H_2O} + y_{O_2,ext} \frac{P_{csm} - \Phi_{csm} P_{sat}(T_{fc})}{P_{csm}} M_{O_2} + (1 - y_{O_2,ext}) \frac{P_{csm} - \Phi_{csm} P_{sat}(T_{fc})}{P_{csm}} M_{N_2}$	(18)
$M_{agc} = \frac{\Phi_{agc} P_{sat}(T_{fc})}{P_{agc}} M_{H_2O} + \frac{P_{agc} - \Phi_{agc} P_{sat}(T_{fc})}{P_{agc}} M_{H_2}$	(19)
$M_i = \frac{\Phi_i P_{sat}(T_{fc})}{P_i} M_{H_2O} + y_{O_2,i} \frac{P_i - \Phi_i P_{sat}(T_{fc})}{P_i} M_{O_2} + (1 - y_{O_2,i}) \frac{P_i - \Phi_{cgc} P_{sat}(T_{fc})}{P_i} M_{N_2}, i \in \{cem, cgc, ext\}$	(20)

Table 5: Synthesis of the molar masses equations

Symbol	Name (Unit)	Value
Auxiliary system model parameters		
τ_{cp}	Air compressor time constant (s)	1 [22]
τ_{hum}	Humidifier time constant (s)	5 [22]
K_p	Proportionality constant of the back pressure valve controller ($m^2 \cdot s^{-1} \cdot Pa^{-1}$)	$5 \cdot 10^{-8}$
K_d	Derivative constant of the back pressure valve controller ($m^2 \cdot Pa^{-1}$)	10^{-8}
C_D	Throttle discharge coefficient	0.05 [22]
$k_{sm,in}$	Nozzle orifice coefficient at the inlet supply manifold ($kg \cdot Pa^{-1} \cdot s^{-1}$)	$1.0 \cdot 10^{-5}$
$k_{sm,out}$	Nozzle orifice coefficient at the outlet supply manifold ($kg \cdot Pa^{-1} \cdot s^{-1}$)	$8.0 \cdot 10^{-6}$ [22]
Auxiliary system physical parameters		
n_{cell}	Number of cells inside the stack	5
V_{sm}	Supply manifold volume (m^3)	$7.0 \cdot 10^{-3}$ [22]
V_{em}	Exhaust manifold volume (m^3)	$2.4 \cdot 10^{-3}$ [22]
A_T	Exhaust manifold throttle area (m^2)	$1.18 \cdot 10^{-3}$ [22]
Physical constants		
γ_{H_2}	Heat capacity ratio of H_2 at 100°C	1.404
γ_a	Heat capacity ratio of dry air at 100°C	1.401
M_{H_2}	Molar mass of H_2 ($kg \cdot mol^{-1}$)	$2 \cdot 10^{-3}$
M_{H_2O}	Molar mass of H_2O ($kg \cdot mol^{-1}$)	$1.8 \cdot 10^{-2}$
M_{O_2}	Molar mass of O_2 ($kg \cdot mol^{-1}$)	$3.2 \cdot 10^{-2}$
M_{N_2}	Molar mass of N_2 ($kg \cdot mol^{-1}$)	$2.8 \cdot 10^{-2}$
External environmental parameters		
T_{ext}	Outside temperature (K)	298
P_{ext}	Outside pressure (Pa)	101325
Φ_{ext}	Outside relative humidity	0.4
$y_{O_2,ext}$	Molar fraction of O_2 in ambient dry air	0.2095

Table 6: Synthesis of the necessary parameters for the balance of plant modeling

Dynamical models	Matter flow expressions
Manifolds at the anode	
$\frac{dP_{asm}}{dt} = \frac{RT_{fc}}{V_{sm}M_{asm}} [W_{asm,in} + W_{are} - n_{cell}W_{asm,out}] \quad (21)$	$W_{asm,in} = k_{sm,in} [P_{a,des} - P_{asm}] \quad (22)$
$\frac{dP_{aem}}{dt} = \frac{RT_{fc}}{V_{em}M_{aem}} [n_{cell}W_{aem,in} - W_{are} - W_{aem,out}] \quad (24)$	$W_{v,asm,in} = \frac{\Phi_{aem}P_{sat}(T_{fc})}{M_{aem}P_{aem}} W_{are} \quad (23)$
$\frac{d\Phi_{asm}}{dt} = \frac{RT_{fc}}{V_{sm}P_{sat}(T_{fc})} [W_{v,asm,in} - J_{v,a,in}H_{gc}W_{gc}n_{cell}] \quad (27)$	$W_{asm,out} = k_{sm,out} [P_{asm} - P_{agc}] \quad (25)$
$\frac{d\Phi_{aem}}{dt} = \frac{RT_{fc}}{V_{em}P_{sat}(T_{fc})} [J_{v,a,out}H_{gc}W_{gc}n_{cell} - W_{v,asm,in} - W_{v,aem,out}] \quad (29)$	$W_{are} = n_{cell}M_{aem} \frac{P_{aem}}{P_{aem} - \Phi_{aem}P_{sat}(T_{fc})} \frac{[S_a - 1][i_{fc} + i_n]A_{act}}{2F} \quad (26)$
	$W_{aem,in} = k_{em,in} [P_{agc} - P_{aem}] \quad (28)$
	$W_{aem,out} = k_{purge} \frac{C_{DA_T}P_{aem}}{\sqrt{RT_{fc}}} \left(\frac{P_{ext}}{P_{aem}} \right)^{\frac{1}{\gamma_{H_2}}} \sqrt{M_{agc} \frac{2\gamma_{H_2}}{\gamma_{H_2} - 1} \left[1 - \left(\frac{P_{ext}}{P_{aem}} \right)^{\frac{\gamma_{H_2}-1}{\gamma_{H_2}}} \right]} \quad (30)$
	$W_{v,aem,out} = \frac{\Phi_{aem}P_{sat}(T_{fc})}{M_{aem}P_{aem}} W_{aem,out} \quad (31)$
Manifolds at the cathode	
$\frac{dP_{csm}}{dt} = \frac{RT_{fc}}{V_{sm}M_{csm}} [W_{csm,in} - n_{cell}W_{csm,out}] \quad (32)$	$W_{csm,in} = W_{cp} + W_{c,inj} \quad (33)$
$\frac{dP_{cem}}{dt} = \frac{RT_{fc}}{V_{em}M_{cem}} [n_{cell}W_{cem,in} - W_{cem,out}] \quad (34)$	$W_{v,csm,in} = \frac{\Phi_{ext}P_{sat}(T_{ext})}{M_{ext}P_{ext}} W_{cp} + \frac{1}{M_{H_2O}} W_{c,inj} \quad (35)$
$\frac{d\Phi_{csm}}{dt} = \frac{RT_{fc}}{V_{sm}P_{sat}(T_{fc})} [W_{v,csm,in} - J_{v,c,in}H_{gc}W_{gc}n_{cell}] \quad (37)$	$W_{csm,out} = k_{sm,out} [P_{csm} - P_{cgc}] \quad (36)$
$\frac{d\Phi_{cem}}{dt} = \frac{RT_{fc}}{V_{em}P_{sat}(T_{fc})} [J_{v,c,out}H_{gc}W_{gc}n_{cell} - W_{v,cem,out}] \quad (39)$	$W_{cem,in} = k_{em,in} [P_{cgc} - P_{cem}] \quad (38)$
	$W_{cem,out} = \frac{C_{DA_{bp,c}}P_{cem}}{\sqrt{RT_{fc}}} \left(\frac{P_{ext}}{P_{cem}} \right)^{\frac{1}{\gamma_a}} \sqrt{M_{cgc} \frac{2\gamma_a}{\gamma_a - 1} \left[1 - \left(\frac{P_{ext}}{P_{cem}} \right)^{\frac{\gamma_a-1}{\gamma_a}} \right]} \quad (40)$
	$W_{v,cem,out} = \frac{\Phi_{cem}P_{sat}(T_{fc})}{M_{cem}P_{cem}} W_{cem,out} \quad (41)$
Air compressor, humidifiers and back-pressure valve	
$\frac{dW_{cp}}{dt} = \frac{W_{cp,des} - W_{cp}}{\tau_{cp}} \quad (42)$	$W_{cp,des} = n_{cell}M_{ext} \frac{P_{ext}}{P_{ext} - \Phi_{ext}P_{sat}(T_{ext})} \frac{1}{y_{O_2,ext}} \frac{S_c [i_{fc} + i_n]A_{act}}{4F} \quad (43)$
$\frac{dW_{c,inj}}{dt} = \frac{W_{c,inj,des} - W_{c,inj}}{\tau_{hum}} \quad (44)$	$W_{c,inj,des} = W_{c,v,des} - W_{v,hum,in} \quad (45)$
$\frac{dA_{bp,c}}{dt} = \begin{cases} 0, & \text{if } A_{bp,c} \geq A_T \text{ and } \frac{dA_{bp,c}}{dt} > 0 \\ 0, & \text{if } A_{bp,c} \leq 0 \text{ and } \frac{dA_{bp,c}}{dt} < 0 \\ -K_p [P_{c,des} - P_{cgc}] + K_d \frac{dP_{cgc}}{dt}, & \text{else} \end{cases} \quad (46)$	$W_{c,v,des} = M_{H_2O} \frac{\Phi_{c,des}P_{sat}(T_{fc})}{P_{cp}} \frac{W_{cp}}{M_{ext}} \quad (47)$
	$W_{v,hum,in} = M_{H_2O} \frac{\Phi_{ext}P_{sat}(T_{ext})}{P_{ext}} \frac{W_{cp}}{M_{ext}} \quad (48)$

Table 7: Synthesis of the differential equations and the associated matter transport expressions in the auxiliary system

2.3. Flaws of this balance of plant model

The model proposed for the auxiliaries has several flaws. First, the only equations in the literature that are practically applicable for calculating the manifold inflow or outflow rates based on a pressure difference are those of the form given in (22), (25), (28), (36) and (38). There are other equations derived from the Bernoulli's principle, such as the one proposed by Pukrushpan [13] and used in (30) and (40). However, these equations, in addition to assuming steady and incompressible flow, which is not valid in the present case, introduce a square root of the pressure difference. This square root function imposes a direction to the flow, as the pressure difference has to be positive, preventing symmetric considerations. This is problematic because, around initial conditions, the flows can be temporarily and briefly reversed. Gas could enter the GC through the outlet manifold, or gas could exit the GC towards the inlet manifold. Square root is also a source of numerical instability when solving the equations. Equations (22), (25), (28), (36) and (38), on the other hand, are obtained by linearizing the aforementioned Bernoulli principle. While it solves the asymmetry issue, the linearization requires that the pressure difference on both sides of the orifice must be very small, which may not be the case in practice. To the best of the authors' knowledge, no superior models for these flows currently exist.

3. Voltage modeling of a PEM cell

3.1. General expressions

The voltage polarization expressions, based on the authors' previous work [26], are adapted for this model and given in table 8. Two significant scientific additions are noteworthy here: κ_{co} and s_{lim} . They have been implemented to enable the model to more accurately simulate reality when comparing results with the experimental data. A discussion dedicated to them can be found in sections 3.2 and 3.3. Finally, general parameters for modeling the cell voltage are furnished in table 9, while the cell's voltage specific parameters contingent upon the cell type used are delineated in section 4.

Voltage polarization expressions	
The apparent voltage	$U_{cell} = U_{eq} - \eta_c - i_{fc} [R_p + R_e]$ (49)
The equilibrium potential	$U_{eq} = E^0 - 8.5 \cdot 10^{-4} [T_{fc} - 298.15] + \frac{RT_{fc}}{2F} \left[\ln \left(\frac{RT_{fc} C_{H_2,ac}}{P_{ref}} \right) + \frac{1}{2} \ln \left(\frac{RT_{fc} C_{O_2,ccl}}{P_{ref}} \right) \right]$ (50)
The overpotential	$\eta_c = \frac{1}{f_{drop}(s, P)} \frac{RT_{fc}}{\alpha_c F} \ln \left(\frac{i_{fc} + i_n}{i_{0,c}^{ref}} \left[\frac{C_{O_2}^{ref}}{C_{O_2,ccl}} \right]^{\kappa_c} \right) \quad (51) \quad s_{lim} = a_{s_{lim}} P_{des} + b_{s_{lim}} \quad (52)$ $f_{drop}(s, P) = \frac{1}{2} \left[1.0 - \tanh \left[\frac{4s_{ccl} - 2s_{lim} - 2s_{switch}}{s_{lim} - s_{switch}} \right] \right] \quad (53) \quad s_{switch} = a_{switch} \cdot s_{lim} \quad (54)$ $\begin{cases} i_{co,H_2} = 2Fk_{H_2}(\lambda_{mem}, T_{fc}) RT_{fc} C_{H_2,ac} \\ i_{co,O_2} = 4Fk_{O_2}(\lambda_{mem}, T_{fc}) RT_{fc} C_{O_2,ccl} \end{cases} \quad (55) \quad i_n = i_{co,H_2} + i_{co,O_2} \quad (56)$
The proton resistance	$R_p = R_{mem} + R_{ccl} \quad (57)$ $R_{mem} = \begin{cases} \frac{H_{mem}}{0.5139 \cdot \lambda_{mem} - 0.326} \exp \left(1268 \left[\frac{1}{303.15} - \frac{1}{T_{fc}} \right] \right), & \text{if } \lambda_{mem} \geq 1 \\ \frac{H_{mem}}{0.1879 \exp \left(1268 \left[\frac{1}{303.15} - \frac{1}{T_{fc}} \right] \right)}, & \text{if } \lambda_{mem} < 1 \end{cases} \quad (58)$ $R_{ccl} = \begin{cases} \frac{H_{ccl}}{\epsilon_{mc}^r [0.5139 \cdot \lambda_{ccl} - 0.326] \exp \left(1268 \left[\frac{1}{303.15} - \frac{1}{T_{fc}} \right] \right)}, & \text{if } \lambda_{ccl} \geq 1 \\ \frac{H_{ccl}}{0.1879 \epsilon_{mc}^r \exp \left(1268 \left[\frac{1}{303.15} - \frac{1}{T_{fc}} \right] \right)}, & \text{if } \lambda_{ccl} < 1 \end{cases} \quad (59)$

Table 8: Synthesis of the voltage polarization expressions

Cell voltage model parameters		
Symbol	Name (Unit)	Value
$C_{O_2,ref}$	Reference concentration of O_2 ($mol.m^{-3}$)	3.39
α_c	Cathode transfer coefficient	0.5
E_0	Standard-state reversible voltage (V)	1.229
P_{ref}	Reference pressure (Pa)	10^5
E_{act}	Activation energy ($J.mol^{-1}$)	$73.2 \cdot 10^3$

Table 9: Synthesis of the general parameters for the cell voltage modeling [26]

3.2. New parameter: the crossover correction coefficient κ_{co}

Expressing the crossover of reactants in fuel cell models is useful for several reasons. First, it is essential for accurately considering the open-circuit voltage in cells and thus obtaining a proper representation of the polarization curve. Furthermore, this information could be valuable to the operator in cases where the cell is temporarily idle. In fact, it is possible to assess the need to flush the anode of any remaining hydrogen, which can lead to cell degradation, when the shutdown is brief and so the quantity of material crossing the membrane is potentially not significant. In such cases, a decision must be made between degradation resulting from purging with ambient air and degradation arising from material crossover.

However, the most notable mathematical expression in the literature, which characterizes this phenomenon, dates back to 2004 [34], as discussed in the authors' previous work [26]. According to the authors' results, this expression is not sufficient to describe the complexity of the crossover in recent stacks. To address this issue, and while awaiting further experiments, the authors propose adding a corrective parameter, denoted here as κ_{co} , to the permeability coefficients of hydrogen and oxygen in the membrane κ_{H_2} and κ_{O_2} . This modification has been directly incorporated into equations (14) and (15). κ_{co} is undetermined and requires calibration to be identified for the specific stack under investigation. Further details on the calibration stage are discussed in section 4.

3.3. New physical quantity: the limit liquid water saturation coefficient s_{lim}

To the authors' knowledge, current models struggle to physically incorporate concentration drop during the simulation of polarization curves. Thus, the most commonly used approach so far does not leverage the fuel cell's physics to explain this drop, but rather involves artificially introducing a new element into the equations. For instance, (60) is a widely known equation which has been used to quantify the concentration voltage loss [13, 35–39]. In this equation, i_{lim} is introduced to define the limit current density at which the concentration drop becomes inevitable. In most studies, i_{lim} is commonly considered as a constant. However, operational conditions invariably influence its value, consequently altering the current density level at which the concentration drop manifests. i_{lim} therefore should be regarded as a function of the operational conditions, for which the link has yet to be identified.

$$U_{conc} = \frac{RT}{2F} \ln \left(\frac{i_{lim}}{i_{lim} - i_{fc}} \right) \quad (60)$$

Next, it is necessary to clarify the use of the coefficient i_{lim} for modeling purposes. As soon as more complex models than lumped-parameter models are employed and internal state data within the catalytic layers are available, the physical representation of i_{lim} changes. It ceases to remain the sole mathematical element in the voltage equations that delineate concentration losses arising from gas diffusion limitations within the cell. This limitation occurs when the concentration of oxygen or hydrogen drops to zero within their respective catalytic layers, and the physical and operating conditions do not permit further supply to this region to counterbalance material consumption at high currents. Indeed, this information is already encompassed within the equilibrium potential and overpotential equations for spatially distributed models, where oxygen and hydrogen concentrations within the catalytic layers can be expressed. This is seen in this work equations (50) and (51). However, in most models, it remains necessary to retain i_{lim} empirically because the current state of the art is not mature enough to take into account all the physical phenomena that impact voltage at high current densities. Indeed, at high currents, liquid water emerges within the cell. This matter subsequently impacts the transport of oxygen and hydrogen to the triple point zones, making it more challenging. This results in a voltage drop [15] for current densities lower than if there were no liquid water present. However, this has not been physically modeled in the existing literature, and i_{lim} serves as an imperfect attempt to

address this because it is detached from the physical variable that explains this phenomenon: the saturation in liquid water s .

Here, we propose a new coefficient, named limit liquid water saturation coefficient s_{lim} , which is indirectly added to the Butler-Volmer equation in (51) to physically consider the impact of catalyst layer flooding on its voltage. U_{conc} is no longer useful. A physical interpretation of this coefficient will be proposed in the authors' future work. This proposition allows for a better connection between the equations and physics, which is valuable as it enables the observation, diagnosis and control of the factor responsible for the concentration drop: s . Additionally, this proposal easily links s_{lim} to operating conditions in (52), which is valuable for considering the stack beyond the arguable optimal conditions imposed by manufacturers.

The proposed contribution here involves adding a new quantity to the Butler-Volmer equation: the liquid water induced voltage drop function f_{drop} . This function, expressed in (53) and shown in figure 3, equals to 0 when the liquid water saturation of the cathodic catalytic layer s_{ccl} exceeds the limit value of s_{lim} , resulting in an increase in overvoltage and, ultimately, a drop in voltage. When s_{ccl} is sufficiently far from this limit, there is no impact of liquid water on the voltage, and therefore, f_{drop} equals 1. In between, f_{drop} strictly decreases towards 0. Indeed, experimentally, the concentration drop is not abrupt and extends over a few tenths of amperes per square centimeter. This is expressed by the fact that liquid water begins to significantly impact the voltage from a certain value of s , and this impact worsens with its increase until the stack stops. Thus, it is necessary to determine a boundary value for s at which the voltage begins to drop, even before reaching s_{lim} . The authors propose considering s_{switch} , which takes a percentage of s_{lim} as the boundary value for the start of voltage drop, as expressed in (54). The proportionality coefficient a_{switch} is an undetermined parameter of the model. Furthermore, f_{drop} is built as a continuous and infinitely differentiable function, which is useful to avoid any fluctuations during numerical resolution.

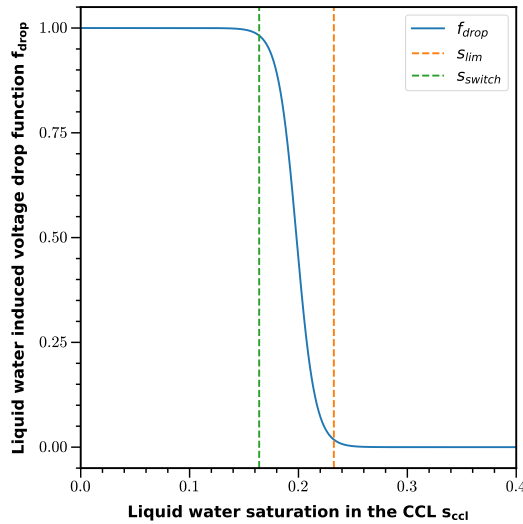


Figure 3: Plot of the liquid water induced voltage drop function, expressed as a function of the liquid water saturation in the CCL, for $P_{des} = 2.5$ bar, $a_{s_{lim}} = 0.05$, $b_{s_{lim}} = 0.1075$ and $a_{switch} = 0.705$

Finally, given that s is interpreted as a hindrance to the arrival of gases in the triple point areas, it is evident that s_{lim} depends on the internal geometry of the stack materials, particularly the GDLs and CLs. Thus, its value inherently relies on the employed technology, making it impossible to establish a universal value. Even a slight modification in the porosity of the stack components would affect it. Therefore, it stands as a parameter specific to fuel cell design. Furthermore, it has been observed that s_{lim} varies with the operating conditions. It is a linear function of the desired gas pressure set by the operator P_{des} , as demonstrated by the model validation section 4. Hence, its proposed expression in (52) involves $a_{s_{lim}}$ and $b_{s_{lim}}$ as two new undetermined parameters. The dependence of s_{lim} on other operating conditions will be studied in future work.

4. Validation of the model's static behavior

The developed model, including the matter flows, the voltage, and the auxiliaries, is implemented in Python. The corresponding programs are organized into a software package named AlphaPEM, which is freely accessible as open-source [40].

To validate the static behavior of the proposed model, a 1 kW EH-31 stack from EH Group [?], dated 2022, was utilized. The physical parameters of the stack, shown in table 10, were either measured in the laboratory or estimated based on conventional dimensions mentioned in the literature [26]. Manufacturers seldom disclose these data; they typically provide only operating conditions. Subsequently, for this validation, experimental data on the same stack for different operational conditions are necessary. Here, polarization curves are employed as reference data. Among the operational conditions, it is the pressure within the stack (equal at the anode and cathode sides: $P_{a,des} = P_{c,des} = P_{des}$) that is altered, while other operational conditions remain constant. Their respective values are listed in table 11.

This validation only concerns the model's static behavior, since it solely relies on data representing the static states of the stack. To assess the dynamism of the model, forthcoming experiments will incorporate electrochemical impedance spectroscopy (EIS) curves. Additionally, this validation remains partial due to its utilization of operating conditions that do not fully capture the diversity of potential states within the stack, as discussed in section 5.3.

Symbol	Accessible physical parameter	Measured value	Estimated value
A_{act}	Active area (m^2)	$8.5 \cdot 10^{-3}$	/
H_{mem}	Membrane thickness (m)	/	$2 \cdot 10^{-5}$
H_{cl}	Catalyst layer thickness (m)	/	10^{-5}
H_{gdl}	Gas diffusion layer thickness (m)	/	$2 \cdot 10^{-4}$
H_{gc}	Gas channel thickness (m)	/	$5 \cdot 10^{-4}$
W_{gc}	Gas channel width (m)	$4.5 \cdot 10^{-4}$	/
L_{gc}	Gas channel cumulated length (m)	9.67	/

Table 10: Synthesis of the accessible physical parameters for the experimental fuel cell

Symbol	Manufacturer operating conditions	Value
T_{fc}	Cell temperature (K)	347.15
P_{des}	Desired cell pressure (4 scenarios) (bar)	1.5 / 2.0 / 2.25 / 2.5
S_a / S_c	Stoichiometries (anode/cathode)	1.2 / 2.0
$\Phi_{a,des} / \Phi_{c,des}$	Desired entrance humidities (anode/cathode)	0.4 / 0.6

Table 11: Synthesis of the manufacturer operating conditions for the EH-31 experimental fuel cell

The model validation process begins by calibrating the undetermined parameters. This calibration involves utilizing two sets of experimental polarization curves derived from the same cell but under distinct operating conditions. These sets serve as a reference for fine-tuning these parameters until achieving convergence between the model's results and the observed experimental outcomes. Here, the maximum voltage deviations ΔU_{max} between the model and experimental curves are below 1.2 %, indicating an excellent calibration. These curves are depicted in figure 4 (the two dashed curves, at 2.0 and 2.25 bar), and their corresponding calibrated values are provided in table 12. Subsequently, the second validation step involves comparing the model outcomes with new experimental data obtained from the same cell, without altering any of the calibrated parameters, under varying operating conditions. It is also noted that the tested data is under operating pressure outside the pressure range used for calibrating the model parameters. The model overfitting can therefore be excluded in the validation phase. Similarly, the maximum voltage deviation ΔU_{max} between the model and experimental curves is low, below 1.8 %. This result is shown in figure 4 (the solid line curve at 2.5 bar). Hence, the model's static behavior has been validated through experimentation.

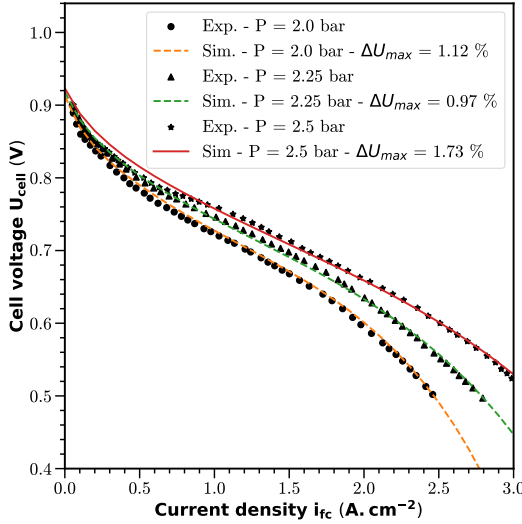


Figure 4: Comparison of polarization curves between simulation and experiment to validate the model's static behavior.

Symbol	Undetermined physical parameters	Calibrated value
$i_{0,c}^{ref}$	Referenced cathode exchange current density ($A.m^{-2}$)	2.79
κ_{co}	Crossover correction coefficient ($mol.m^{-1}.s^{-1}.Pa^{-1}$)	27.2
κ_c	Overpotential correction exponent	1.61
τ	Pore structure coefficient	1.02
ε_{mc}	volume fraction of ionomer in the CLs	0.399
R_e	Electron conduction resistance ($\Omega.m^2$)	$5.70 \cdot 10^{-7}$
ϵ	Capillary exponent	5
ε_c	GDL compression ratio	0.271
ε_{gdl}	GDL porosity	0.701
$a_{slim}, b_{slim}, a_{switch}$	$slim$ coefficients ($bar^{-1}, \emptyset, \emptyset$)	0.0555, 0.1051, 0.63654

Table 12: Synthesis of the calibrated undetermined parameters for the EH-31 experimental fuel cell

5. Results analysis

5.1. Tracking internal states

Under an arbitrary dynamic operating condition, the developed model enables monitoring within a cell of the water evolution, whether in the form of vapor, liquid, or dissolved matter in the membrane, characterized respectively by the variables C_v , s , or λ . It also tracks the evolution of dihydrogen, dioxygen, and nitrogen, characterized by the variables C_{H_2} , C_{O_2} , and C_{N_2} . These variables are evaluated at several nodes within the cell, and the variables with indices agdl or cgdl refer to the node in the center of the corresponding GDL. Additionally, data regarding matter flows between these nodes (J) are also accessible. Furthermore, the evolution of pressures P and humidities Φ within the auxiliary manifolds can also be tracked. Finally, the cell voltage over time U_{cell} is calculated from these internal states.

Several results of the calibrated model are shown in figures 5, 6 and 8, under pressure $P_{des} = 2.0$ bar. In this study case, a step-shape current density is applied, ranging from $0 A.cm^{-2}$ to $0.5 A.cm^{-2}$ at the start of the experiment, and then from $0.5 A.cm^{-2}$ to $1.5 A.cm^{-2}$ at $500s$, as seen in figure 5a. The variables are initialized to the values they would have in steady-state conditions, with zero current density, if they were subjected to the pressure, humidity, and temperature of the desired operating conditions. For simplicity, it is assumed that the variables within each cell are initially subject to the average of the anodic and cathodic pressures and humidity. The experiment virtually lasts $1000s$.

The advantage of performing a double step-shape current density is to eliminate the need for initial condition values in the analysis of the results. Indeed, the first step-shape current density allows the system to reach a steady state within the fuel cell, with a waiting time of 500 seconds. Since the fuel cell is controlled, it will always reach the same steady state regardless of its initial conditions, which only influence its transition to this stationary state. Thus, after around 500 seconds, the fuel cell operates in a state with realistic internal values. The second step-shape current density can then be studied under standardized conditions.

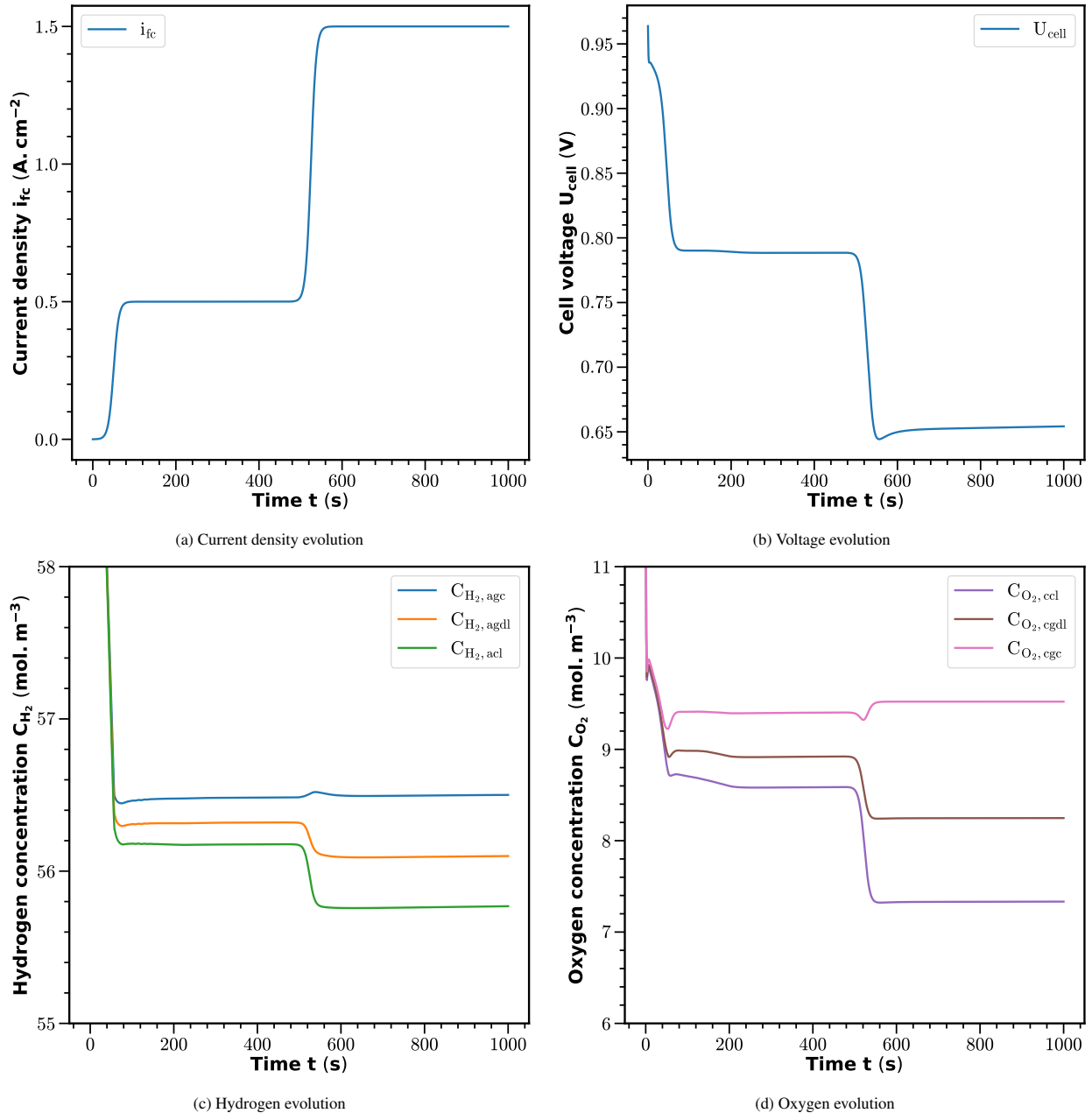


Figure 5: Internal states of a PEM fuel cell system for two current density steps, computed by AlphaPEM (1/3).

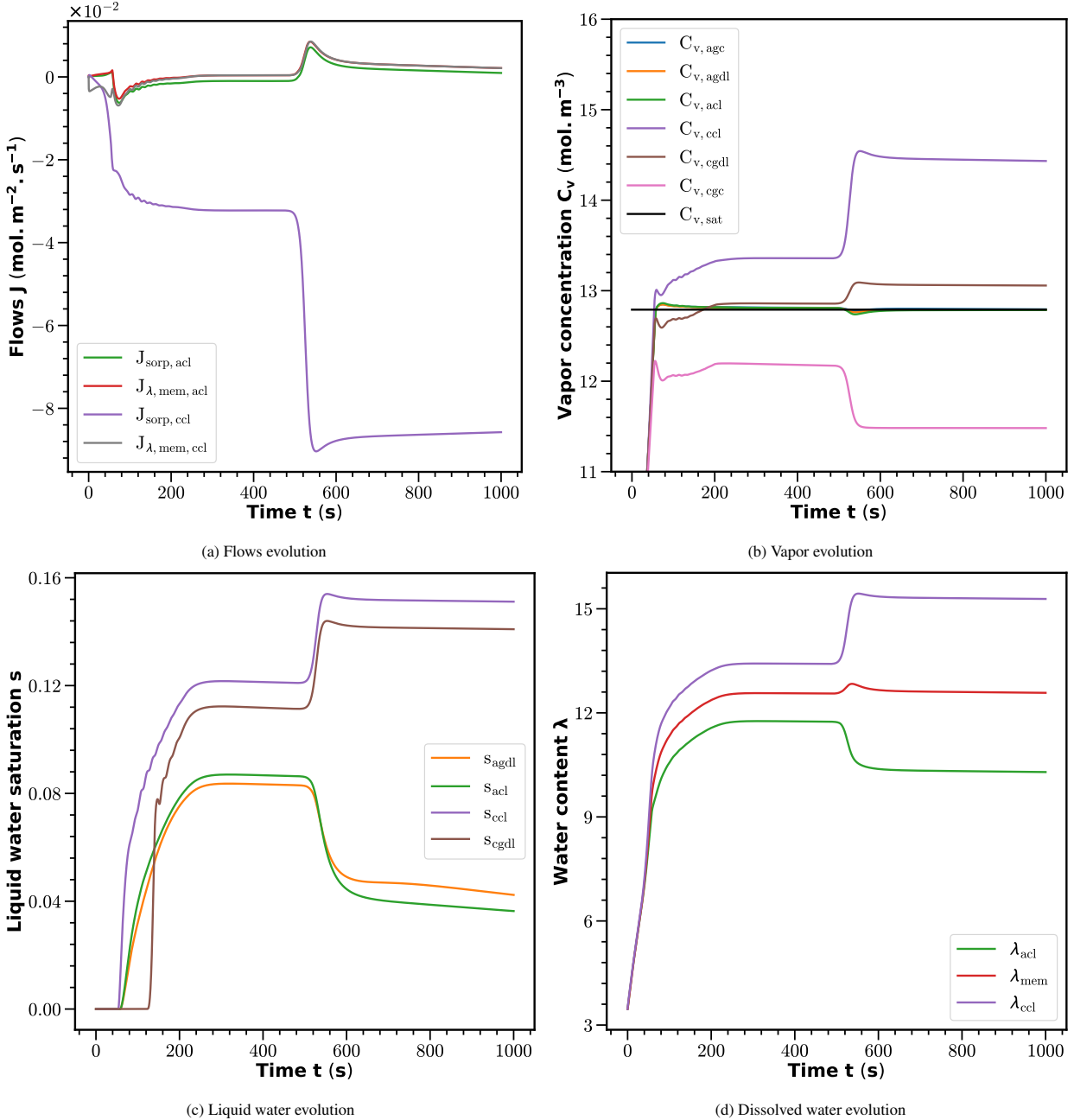


Figure 6: Internal states of a PEM fuel cell system for two current density steps, computed by AlphaPEM (2/3).

The results generally follow the expected pattern within the cell: an increase in current density leads to increased flows, reduced reactants, and increased water content. However, it is necessary to further examine certain variables to clarify their behavior. Firstly, the reactants in the bipolar plates, characterized by $C_{H_2,agc}$ and $C_{O_2,cgc}$ figures 5c and 5d, do not exhibit significant changes and tend to slightly increase, unlike the reactants in the membrane electrode assembly (MEA) $C_{H_2,agdl}$, $C_{H_2,acl}$, $C_{O_2,cgdl}$ and $C_{O_2,ccl}$. This can be explained by the fact that $C_{H_2,agc}$ and $C_{O_2,cgc}$ are less sensitive to the chemical activity within the MEA, as the stack is designed to stabilize the pressure within the bipolar plates using a backpressure valve. The slight fluctuations are attributed to changes in the composition of this gas mixture, with a decrease in vapor concentration ($C_{v,agc}$ and $C_{v,cgc}$ figure 6b) occurring at high currents due to its

expulsion by the increased gas flow rates involved.

Then, it is surprising that the behavior of water at the anode differs from that at the cathode, regardless of its form (vapor with $C_{v,agdl}$ and $C_{v,acl}$ figure 6b, liquid with s_{agdl} and s_{acl} figure 6c, or dissolved with λ_{agdl} and λ_{acl} figure 6d): it decreases with current density (except at low currents $< 0.5 \text{ A.cm}^{-2}$ where it increases with current density, even after leaving the initial state). This can be explained by the existence of two opposing phenomena. On one hand, more water is created at the cathode with increasing current and passes through the membrane towards the anode. On the other hand, the flow of gases circulating in the bipolar plates also increases, making it easier to remove water from the MEA. As these flows are of the same order of magnitude, it is not easy to predict the evolution of water vapor in the anode. This depends on several parameters, such as the stoichiometry and geometric parameters like the thicknesses of the membrane and the thicknesses of the MEA. To illustrate this point, the same experiment was repeated with a threefold reduction in the thickness of the membrane and the catalytic layer, significantly reducing the resistance of the membrane to the passage of water from the cathode to the anode. Thus, the decrease in liquid water at the anode side is no longer visible and has been replaced by an increase, as shown in Figure 7.

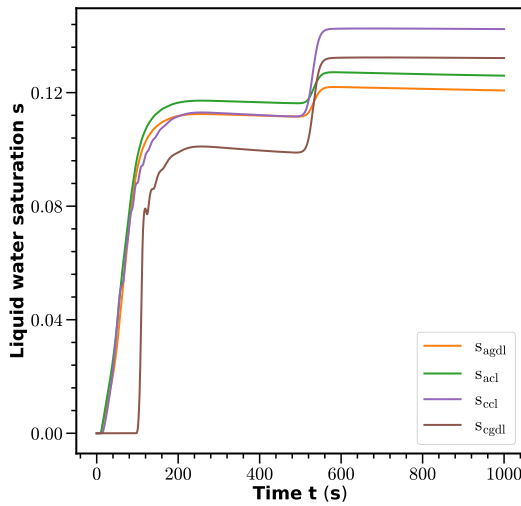


Figure 7: Evolution of liquid water within the cell for a membrane and a catalytic layer three times thinner.

Furthermore, the impact of auxiliary dynamics is particularly evident in the evolution of oxygen concentrations with $C_{O_2,cgc}$ figure 5d, or equivalently P_{cgc} figure 8a (which influences $C_{O_2,cgdl}$ and $C_{O_2,ccl}$), leading to fluctuations in concentrations with each change in current density. This phenomenon does not occur when the cell is modeled without auxiliaries. However, in this model, the other variables are less affected than $C_{O_2,cgc}$ by the presence of auxiliaries.

However, there is a fluctuation in most internal states when a current density step is crossed, especially concerning water (see $C_{v,ccl}$ figure 6b for example). It is characterized by a slight overshoot in the equilibrium value. This can be explained by the sudden increase in current that causes a sudden production of water in the cell. The discharge of this water is not sudden and possesses some inertia, leading to a transient over-accumulation of matter, namely a peak. This observed dynamic phenomenon is of interest, considering that the amount of water can affect the cell's voltage and potentially damage it. Thus, in energy management strategies, it might be interesting to slow down this increase in current density attributed to the fuel cell by temporarily compensating the energy demand with other electricity sources, such as batteries. Consequently, these observed peaks will disappear.

Next, liquid water saturation sometimes evolves with slight fluctuations, notably observed figure 6c around 200s for s_{ccl} and s_{cgdl} . These fluctuations subsequently impact other variables, such as $C_{v,cgdl}$, $C_{v,cgc}$, $S_{sorp,acl}$, $J_{\lambda,mem,acl}$, $S_{sorp,ccl}$, and $J_{\lambda,mem,ccl}$. These are minor numerical errors resulting from an insufficiently high number of nodes in each GDL, as discussed in section 1.1.1. Here, it was chosen not to use an excessively high number of nodes to avoid significantly increasing computation times, even at the cost of a slight loss in precision in the results. Indeed, quadrupling n_{gdl} is necessary to achieve nearly perfectly smooth results, which triples the computation times.

It is also noteworthy to observe that water vapor concentrations C_v can exceed the saturation vapor value $C_{v,sat}$

figure 6b. This can be explained by the dynamic equilibrium at stake. On one hand, surpassing the water vapor saturation threshold triggers the condensation of this vapor into liquid water. However, this condensation is not instantaneous and depends on a time constant γ_{cond} embedded within the model. On the other hand, the stack continues to produce large amounts of water that feed into the water vapor. Indeed, in this model, it has been assumed that water production occurs necessarily in a dissolved manner. The current state of research does not allow us to determine in what form water appears immediately after the chemical redox reaction between hydrogen and oxygen [26, 31]. A choice must therefore be made. Furthermore, in this model, the water flows between the membrane and the catalytic layer necessarily occur between a dissolved form and a vapor form. Only thereafter is condensation possible. Water production in the cell therefore directly involves vapor water supply. The supply flow of water vapor and condensation thus oppose each other, resulting in a dynamic equilibrium that can exceed the saturation vapor point, as long as the cell operates. If the time constant associated with condensation, γ_{cond} , is increased sufficiently, this phenomenon disappears, and C_{sat} becomes the actual limit of the water vapor concentration. However, the value chosen for γ_{cond} in the authors' model corresponds to that recommended by Hua Meng in a dedicated study [41]. Thus, this oversaturation phenomenon is acceptable.

Inside the auxiliaries, it is also remarkable to note that the pressure difference between the manifolds and the bipolar plates, shown figure 8a, is low in this model, on the order of 1 to 10Pa, which is not realistic. This stems, on the one hand, from the unmodeled pressure losses, and on the other hand, from the choice of equations (22), (25), (28), (36), and (38) which concern the incoming or outgoing matter flows from the manifolds and are based on simplifying assumptions. This is an aspect that needs improvement in the model.

Moreover, it is interesting to discuss the evolution of humidity in the auxiliaries, as shown in the curve 8b. The supply manifold receives a controlled water flow which is at the desired humidity level, while also delivering a water flow to the cell. It stabilizes at a value lower than the desired humidity. This is a consequence of the chosen humidity control strategy, which focuses on the water flow entering the supply manifold rather than the humidity level within the supply manifold itself. Additionally, it can be observed that the humidity in the exhaust manifold stabilizes at the same level as the humidity in the gas channel. This humidity also corresponds to that of the flow exiting the cell, as the current model is one-dimensional.

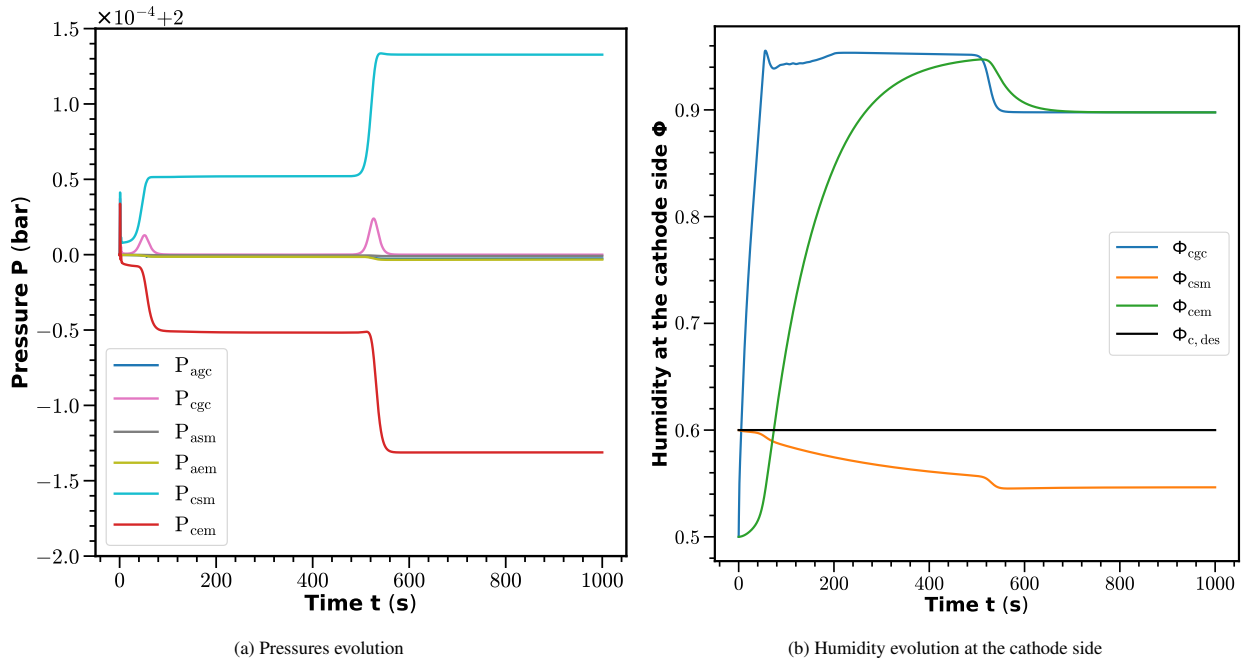


Figure 8: Internal states of a PEM fuel cell system for two current density steps, computed by AlphaPEM (3/3).

5.2. AlphaPEM computational efficiency

This 1000s simulation was conducted on a workstation featuring an Intel Core i9-11950H @ 2.60 GHz processor and required 17s of computation time. Simulating a polarization curve takes 9s. Therefore, the model implemented within AlphaPEM operates within the same order of magnitude as other 1D simulators mentioned in the literature [24], is two orders of magnitude faster than a 1D model from commercial software like Comsol Multiphysics [24], and four to five orders of magnitude faster than 1D+1D, 3D+1D, or 3D models from the literature [10, 19, 42]. The computation times obtained by AlphaPEM are thus compatible with uses in embedded applications. It is important to note that while the model's computational speed is significantly enhanced, its precision is inherently lower compared to models simulating higher dimensional spaces.

5.3. Limits of the model

Despite the excellent agreements observed in section 4 between the experimental and model results at pressures of 2.0, 2.25, and 2.5 bar, the comparison is less favorable at a lower pressure of 1.5 bar, as illustrated in figure 9. Specifically, the error remains low for current densities below 1.3 A.cm^{-2} , with $\Delta U_{max} = 1.52 \%$ within this range, but increases significantly for higher current densities.

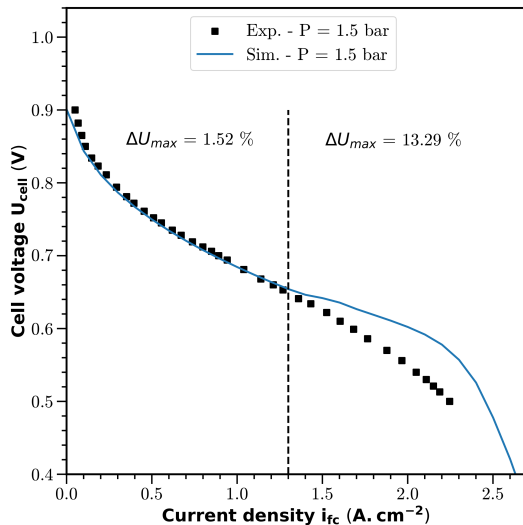


Figure 9: Comparison of polarization curves between simulation and experiment at 1.5 bar.

This variation arises from the condensation of water within the cell, starting exactly from $i_{fc} = 1.3 \text{ A.cm}^{-2}$, whereas liquid water was consistently present for all current density levels in previous experiments. It is plausible that the limited theoretical understanding of water sorption in catalytic layers, as criticized in the authors' prior work [26], causes inaccurate simulation of the transition from a humid gas without condensed water to a gas saturated with vapor and with liquid water. This could result in the significant errors observed in this simulated voltage. Thus, the authors urge the scientific community to enhance the theory describing the evolution of water in its various states within each cell.

It is also conceivable that this deviation arises from the methodology employed by stack manufacturers in experimentally measuring the polarization curve. If the measurement is conducted dynamically rather than statically, it could impact the results. Dynamic measurement of the polarization curve involves initially balancing the stack at a nominal operating point, then rapidly sweeping through the entire current density range without achieving perfect equilibrium for each current density. Consequently, if the stack lacks adequate time for proper balancing, the amount of liquid water at a given current density might differ compared to a static scenario, resulting in disparities in the measured concentration drop. This effect could be particularly pronounced at a pressure of 1.5 bar, as the nominal operating point might not initially yield liquid water, for instance, if set at 1.0 A.cm^{-2} , unlike in other considered scenarios.

Hence, new polarization curve tests with assured equilibrium at each current density point would be imperative to verify this hypothesis.

Additionally, it is crucial to acknowledge the limited scope of validating a PEM fuel cell model solely based on three polarization curves. These curves, which vary only in pressure from 2.0 to 2.5 bar, fail to encompass the full range of physical scenarios occurring within one cell. Indeed, the transition between a humid gas without liquid water and a gas saturated with vapor containing liquid water is notably absent with these operating conditions. Consequently, the accuracy of the results is contingent upon specific conditions, rendering the model unreliable for all scenarios. It would be beneficial to develop a routine, under specified operating conditions, that ensures comprehensive coverage of all relevant physical phenomena within the cell, for its static validation with polarization curves.

6. Conclusion

Multi-physics models allow increasing the available information to better control PEM fuel cells, which is valuable considering the impossibility of placing sensors inside a cell. Currently, most existing models either provide a very detailed description of the internal states of the cell but require a very high computational cost, such as computational fluid dynamics models, or are fast but provide summary information about the cell, such as lumped-parameter models.

This work aims to find a better compromise to combine result accuracy and execution speed. Thus, a one-dimensional, dynamic, two-phase, isothermal, and finite-difference model of the PEMFC system has been developed, and its static behavior has been validated against several published experimental polarization curves. This model runs two orders of magnitude faster than 1D models from the commercial software Comsol Multiphysics and up to five orders of magnitude faster than 3D models from the literature. It remains compatible with embedded applications and provides more precision than lumped-parameter models.

In addition, a new coefficient has been introduced to replace the limit current density coefficient (i_{lim}). This coefficient, the limit liquid water saturation coefficient (s_{lim}), also determines the voltage drop at high current densities. s_{lim} offers the added advantage of establishing a physical connection between this voltage drop, the internal states of the cell, and the operating conditions. Moreover, this parameter has been proven to be a function of the pressure imposed by the operators P_{des} .

In upcoming researches, experimental verification will be conducted to determine whether s_{lim} is dependent on other operating conditions, such as the temperature T_{fc} , and a physical interpretation of this coefficient will be proposed. Additionally, the model will undergo refinement through the incorporation of heat exchange modeling, the extension to a "1D+1D" model and the simulation of electrochemical impedance spectroscopy curves, all while maintaining computational efficiency. Further attention will be given to enhancing the control design of the model. Finally, the algorithm for this fuel cell model, released as open-source software and named AlphaPEM, will serve as a robust tool for future researchers needing a modifiable complex physics-based model for their investigations.

7. Acknowledgments

This work has been supported by French National Research Agency via project DEAL (Grant no. ANR-20-CE05-0016-01), the Region Provence-Alpes-Côte d'Azur, the EIPHI Graduate School (contract ANR-17-EURE-0002) and the Region Bourgogne Franche-Comté.

Nomenclature

Physical quantities

A_{act}	active area (m^2)
A_T	exhaust manifold throttle area (m^2)
a_w	water activity in the pores of the CL
C	molar concentration ($mol.m^{-3}$)
C_D	throttle discharge coefficient

D	diffusion coefficient of water in the membrane ($m^2.s^{-1}$)
$D_{i/j}$	binary diffusivity of two species i and j in open space ($m^2.s^{-1}$)
E^0	standard-state reversible voltage (V)
E_{act}	activation energy ($J.mol^{-1}$)
F	Faraday constant ($C.mol^{-1}$)

f_{drop}	liquid water induced voltage drop function	s	liquid water saturation
f_v	water volume fraction of the membrane	s_{lim}	limit liquid water saturation coefficient
H	thickness (m)	α_c	charge-transfer coefficient of the cathode
h	convective-conductive mass transfer coefficient (m.s ⁻¹)	η	overpotential (V)
i	current density per unit of cell active area (A.m ⁻²)	$\gamma_{cond}/\gamma_{evap}$	overall condensation/evaporation rate constant for water (s ⁻¹ /Pa ⁻¹ .s ⁻¹)
i_n	internal current density (A.m ⁻²)	γ_{H_2}/γ_a	heat capacity ratio of H ₂ and dry air
i_{lim}	limit current density coefficient	γ_{sorp}	sorption rate (s ⁻¹)
J	molar/mass transfer flow (mol.m ⁻² .s ⁻¹ /kg.m ⁻² .s ⁻¹)	κ_c	overpotential correction exponent
K	permeability (m ²)	κ_{co}	crossover correction coefficient
k	permeability coefficient in the membrane	λ	water content
K_p/K_d	proportionality/derivative constant of the back pressure valve controller (m ² .s ⁻¹ .Pa ⁻¹ /m ² .Pa ⁻¹)	ν_l	liquid water kinematic viscosity (m ² .s ⁻¹)
$k_{i,j}$	nozzle orifice coefficient for i ∈ {sm, em} and j ∈ {in, out} (kg.Pa ⁻¹ .s ⁻¹)	Φ	relative humidity
L_{gc}	cumulated length of the gas channel (m)	ρ	density (kg.m ⁻³)
M	molecular weight (kg.mol ⁻¹)	σ	surface tension of liquid water (N.m ⁻¹)
n	number of moles (mol)	τ	pore structure coefficient
n_{cell}	number of cells inside the simulated stack	τ_{cp}/τ_{hum}	air compressor/humidifier time constant (s)
n_{gdl}	number of nodes inside each GDL	θ_c	contact angle of GDL for liquid water (°)
P	pressure (Pa)	ε	porosity
R	universal gas constant (J.mol ⁻¹ .K ⁻¹)	ε_c	compression ratio
R_e/R_p	electron/proton conduction resistance (Ω.m ²)	ε_{mc}	volume fraction of ionomer in the CLs
r_f	carbon fiber radius (m)	ε_p	percolation threshold porosity
S	matter conversion (mol.m ⁻³ .s ⁻¹)		Mathematical symbols
S_a/S_c	stoichiometric ratio at the anode/cathode	\mathbf{i}	unit vector along the x-axis
S_h	Sherwood number	K_{shape}	shape mathematical factor
S_{vl}	phase transfer rate of condensation and evaporation (mol.m ⁻³ .s ⁻¹)	α, β_1, β_2	fitted values for K_0
T_{fc}	fuel cell temperature (K)	$a_{s_{lim}}, b_{s_{lim}}, a_{switch}, s_{switch}$	fitted values for f_{drop}
U	voltage (V)	∇	gradient notation
V	molar volume (m ³ .mol ⁻¹)		Subscripts and superscripts
V_{sm}/V_{em}	manifold volume (m ³)	a	anode
W	mass flow rate (kg.s ⁻¹ /mol.s ⁻¹)	aem	anode exhaust manifold
W_{gc}	width of the gas channel (m)	asm	anode supply manifold
x	space variable (m)	c	cathode
x_v	mole fraction of vapor	cem	cathode exhaust manifold
y_{O_2}	molar fraction of O ₂ in dry air	co	crossover
ϵ	capillary exponent	cp	compressor
		csm	cathode supply manifold
		eff	effective
		eq	equilibrium
		fc	fuel cell
		H_2	dihydrogen

		Abbreviation
<i>in</i>	inlet	
<i>l</i>	liquid	<i>acl/ACL</i> anode catalyst layer
<i>mem</i>	membrane	<i>agc/AGC</i> anode gas channel
<i>N</i> ₂	dinitrogen	<i>agdl/AGDL</i> anode gas diffusion layer
<i>O</i> ₂	dioxygen	<i>ccl/CCL</i> cathode catalyst layer
<i>out</i>	outlet	<i>cgc/CGC</i> cathode gas channel
<i>p</i>	production	<i>cgdl/CGDL</i> cathode gas diffusion layer
<i>ref</i>	referenced	<i>cl/CL</i> catalyst layer
<i>sat</i>	saturated	<i>EOD</i> electro-osmotic drag
<i>sorp</i>	sorption	<i>gc/GC</i> gas channel
<i>v</i>	vapor	<i>gdl/GDL</i> gas diffusion layer
<i>vl</i>	vapor to liquid	<i>PEMFC</i> proton exchange membrane fuel cell
<i>w</i>	water	

References

- [1] E. Union, Clean Hydrogen Joint Undertaking. Strategic Research and Innovation Agenda 2021 – 2027 (2022).
- [2] K. Jiao, J. Xuan, Q. Du, Z. Bao, B. Xie, B. Wang, Y. Zhao, L. Fan, H. Wang, Z. Hou, S. Huo, N. P. Brandon, Y. Yin, M. D. Guiver, Designing the next generation of proton-exchange membrane fuel cells, *Nature* 595 (7867) (2021) 361–369, cet article est orienté vers l'amélioration de la densité de puissance de la pile PEMFC. doi:10.1038/s41586-021-03482-7.
- [3] Fei Gao, B. Blunier, A. Miraoui, A. El Moudni, A Multiphysics Dynamic 1-D Model of a Proton-Exchange-Membrane Fuel-Cell Stack for Real-Time Simulation, *IEEE Trans. Ind. Electron.* 57 (6) (2010) 1853–1864. doi:10.1109/TIE.2009.2021177.
- [4] J. Luna, S. Jemei, N. Yousfi-Steiner, A. Husar, M. Serra, D. Hissel, Nonlinear predictive control for durability enhancement and efficiency improvement in a fuel cell power system, *Journal of Power Sources* 328 (2016) 250–261, le compresseur est plutôt finement modélisé. Il calcule assez précisément l'efficacité globale du système pile à combustible, avec les auxiliaires. Il y a aussi une discussion sur la dégradation du platine. doi:10.1016/j.jpow sour.2016.08.019.
- [5] H. Wu, Mathematical Modeling of Transient Transport Phenomena in PEM Fuel Cells, Ph.D. thesis, modélisation 3D de la pile. Ca utilise le CFD (Computational Fluid Dynamic) et c'est très compliqué. C'est un modèle dynamique 3-D, avec considérations de la thermique et avec 2 phases, sans vieillissement (2009).
- [6] L. Fan, G. Zhang, K. Jiao, Characteristics of PEMFC operating at high current density with low external humidification, *Energy Conversion and Management* 150 (2017) 763–774, ce document a été relativement bien cité, il a l'air bien fiable. Jiao est co-auteur. Il m'est utile pour confirmer la valeur de constantes, d'équations et m'apporte une nouvelle équation : la viscosité dynamique de l'eau fonction de la température. Il me permet aussi d'avoir une très bonne expression de la surtension. “sufficient external humidification is necessary to prevent the polymer electrolyte dehydration at low current density, while at high current density, the water produced in cathode CL is enough to humidify the polymer electrolyte” Takalloo et al. [17] indicated that the external humidification at anode inlet was more necessary than the cathode inlet, because the cathode could produce water and should avoid from flooding. En fonction de l'humidité relative d'entrée, les flux d'eau entre GDL et GC ont une direction différente, et cette direction peut varier le long du GC ! J'ai aussi ici des informations utiles sur les vitesses en jeu et leur répartition spatiale. doi:10.1016/j.enconman.2017.08.034.
- [7] B. Xie, G. Zhang, Y. Jiang, R. Wang, X. Sheng, F. Xi, Z. Zhao, W. Chen, Y. Zhu, Y. Wang, H. Wang, K. Jiao, “3D+1D” modeling approach toward large-scale PEM fuel cell simulation and partitioned optimization study on flow field, *eTransportation* 6 (2020) 100090, article intéressant qui montre une faible pente dans la courbe de pola alors que du 3D+1D est utilisé comme modèle. Donne des informations sur les paramètres de la MPL. doi:10.1016/j.etran.2020.100090.
- [8] C. Robin, M. Gerard, J. d'Arbigny, P. Schott, L. Jabbour, Y. Bultel, Development and experimental validation of a PEM fuel cell 2D-model to study heterogeneities effects along large-area cell surface, *International Journal of Hydrogen Energy* 40 (32) (2015) 10211–10230, modélisation 2D+1D qui considère la thermique. Cependant la partie modélisation est dure à comprendre. doi:10.1016/j.ijhydene.2015.05.178.
- [9] J. O. Schumacher, J. Eller, G. Sartoris, T. Colinart, B. C. Seyfang, 2+1D modelling of a polymer electrolyte fuel cell with glassy-carbon microstructures, *Mathematical and Computer Modelling of Dynamical Systems* 18 (4) (2012) 355–377, article conseillé par Zhongliang sur la modélisation 2+1D. doi:10.1080/13873954.2011.642390.
- [10] E. Tardy, J.-P. Poirot-Crouvezier, P. Schott, C. Morel, G. Serre, Y. Bultel, Investigation of liquid water heterogeneities in large area proton exchange membrane fuel cells using a Darcy two-phase flow model in a multiphysics code, *International Journal of Hydrogen Energy* 47 (91) (2022) 38721–38735, une comparaison est faite avec un modèle 1D. Ils ont de meilleurs résultats malgré un temps de calcul élevé. La version éditeur n'est pas encore sortie sur Libgen. Ici j'ai la version HAL. doi:10.1016/j.ijhydene.2022.09.039.
- [11] M. Mayur, S. Strahl, A. Husar, W. G. Bessler, A multi-timescale modeling methodology for PEMFC performance and durability in a virtual

fuel cell car, International Journal of Hydrogen Energy 40 (46) (2015) 16466–16476, article conseillé par Zhongliang qui traite d'un modèle 2D. Zhongliang le trouve très cohérent.
 Il y a aussi de bonnes considérations de dégradation sur la membrane. Un modèle simple a été employé pour prouver la faisabilité du modèle.
 doi:10.1016/j.ijhydene.2015.09.152.

[12] C. Bao, W. G. Bessler, Two-dimensional modeling of a polymer electrolyte membrane fuel cell with long flow channel. Part I. Model development, Journal of Power Sources 275 (2015) 922–934, semble être un excellent document sur la modélisation 2D.
 L'idée est exactement la même que la mienne en 1D+1D, sauf qu'il y a une connection entre les points à l'intérieur de la pile.
 Source 26 de l'article 2021 de Ling Xu afin d'obtenir une équation expérimentale décrivant l'équilibre de l'eau au niveau de la membrane.
 doi:10.1016/j.jpowsour.2014.11.058.

[13] J. T. Pukrushpan, H. Peng, A. G. Stefanopoulou, Control-Oriented Modeling and Analysis for Automotive Fuel Cell Systems, Journal of Dynamic Systems, Measurement, and Control 126 (1) (2004) 14–25. doi:10.1115/1.1648308.

[14] M. Grimm, M. Hellmann, H. Kemmer, S. Kabelac, Water Management of PEM Fuel Cell Systems Based on the Humidity Distribution in the Anode Gas Channels, Fuel Cells 20 (4) (2020) 477–486. doi:10.1002/fuce.202000070.

[15] O. Lottin, B. Antoine, T. Colinart, S. Didierjean, G. Maranzana, C. Moyne, J. Ramousse, Modelling of the operation of Polymer Exchange Membrane Fuel Cells in the presence of electrodes flooding, International Journal of Thermal Sciences 48 (1) (2009) 133–145. doi:10.1016/j.ijthermalsci.2008.03.013.

[16] O. Shamardina, A. A. Kulikovsky, A. V. Chertovich, A. R. Khokhlov, A Model for High-Temperature PEM Fuel Cell: The Role of Transport in the Cathode Catalyst Layer, Fuel Cells 12 (4) (2012) 577–582. doi:10.1002/fuce.201100144.

[17] B. Wang, K. Wu, Z. Yang, K. Jiao, A quasi-2D transient model of proton exchange membrane fuel cell with anode recirculation, Energy Conversion and Management 171 (2018) 1463–1475, ces trois articles sont issus de la même équipe.
 Si j'ai bien compris, Bowen Wang créé un modèle 1D+1D avec considérations de la thermique et Zirong Yang l'utilise sous différentes manières.
 DEA (dead-ended anode) : « local hydrogen concentration near the anode exit would approach to zero caused by nitrogen and liquid accumulation about **300–600 s** operating time, and the time was mainly determined by the operating current density [Yesilyurt et al.]. »
 Cette chute locale en concentration dégrade aussi localement la pile par corrosion du carbone.
 “membrane dehydration was the main reason for performance degradation during purge [Chen et al.].”
 “The pressure drop along the channel can neglected for 10 cm-long straight channels [5,27].”
 “The hydrogen circulating pump can fully recycle the exhaust gas, including hydrogen, nitrogen and vapor, and well mix with purge hydrogen. The cycle interval is assumed as 0.01 s. The exhaust liquid can be separated and removed by the pump.”
 “Liquid water volume fraction is fixed to zero for flow-through channel because liquid can be blown away quickly by the flow.”
 Nitrogen crossover is given here.
 “the surface electric potential in each segment is the same”
 Pour la 1D+1D, seulement 5 points sont pris dans le GC, car d'après eux il y a peu de différences à choisir plus de points et donc c'est un bon compromis temps/précision.
 “The temperature distribution of the fuel cell fits the local current density distribution at equilibrium. The temperature at cathode downstream is higher than upstream. The temperature difference between the catalyst layer and the channel is only about 3 °C because the good cooling effect is assumed in the model.”. doi:10.1016/j.enconman.2018.06.091.

[18] Z. Yang, Z. Liu, L. Fan, Q. Du, K. Jiao, Modeling of Proton Exchange Membrane Fuel Cell System Considering Various Auxiliary Subsystems, in: A. Vasel, D. S.-K. Ting (Eds.), The Energy Mix for Sustaining Our Future, Springer International Publishing, Cham, 2019, pp. 18–33, ces trois articles sont issus de la même équipe.
 Si j'ai bien compris, Bowen Wang créé un modèle 1D+1D avec considérations de la thermique et Zirong Yang l'utilise sous différentes manières. doi:10.1007/978-3-030-00105-6_2.

[19] Z. Yang, K. Jiao, Z. Liu, Y. Yin, Q. Du, Investigation of performance heterogeneity of PEMFC stack based on 1+1D and flow distribution models, Energy Conversion and Management 207 (2020) 112502, ces trois articles sont issus de la même équipe.
 Si j'ai bien compris, Bowen Wang créé un modèle 1D+1D avec considérations de la thermique et Zirong Yang l'utilise sous différentes manières.
 Ici il s'agit à priori d'un modèle 1D+1D d'un stack, et pas d'une cellule.
 L'une des dimensions correspond à l'empilement des cellules.
 À vérifier car il faut se baser sur leurs travaux précédents pour en être sûr.
 Un gros travail est fait sur les pertes de charges. doi:10.1016/j.enconman.2020.112502.

[20] D. Falcão, V. Oliveira, C. Rangel, C. Pinho, A. Pinto, Water transport through a PEM fuel cell: A one-dimensional model with heat transfer effects, Chemical Engineering Science 64 (9) (2009) 2216–2225. doi:10.1016/j.ces.2009.01.049.

[21] D. Falcão, C. Pinho, A. Pinto, Water management in PEMFC: 1-D model simulations, Ciência & Tecnologia dos Materiais 28 (2) (2016) 81–87, modélisation 1D de la pile avec ajout de la thermique. doi:10.1016/j.ctmat.2016.12.001.

[22] L. Xu, J. Hu, S. Cheng, C. Fang, J. Li, M. Ouyang, W. Lehnert, Robust control of internal states in a polymer electrolyte membrane fuel cell air-feed system by considering actuator properties, International Journal of Hydrogen Energy 42 (18) (2017) 13171–13191, article directement utilisé par Ling Xu pour construire son modèle d'auxiliaires.
 Donne une expression expérimentale pour calculer $W_{cp} = f(w_{cp}, P_{u/d})$. doi:10.1016/j.ijhydene.2017.03.191.

[23] Y. Shao, L. Xu, X. Zhao, J. Li, Z. Hu, C. Fang, J. Hu, D. Guo, M. Ouyang, Comparison of self-humidification effect on polymer electrolyte membrane fuel cell with anodic and cathodic exhaust gas recirculation, International Journal of Hydrogen Energy 45 (4) (2020) 3108–3122, article directement utilisé par Ling Xu pour construire son modèle d'auxiliaires.
 Il est bien écrit et est un bon modèle pour faire un article.
 Il y a quelques valeurs pour les coefficients des orifices des collecteurs, des données supplémentaires sur les purges, des données sur la condensation de l'eau lors du mélange entre gaz "frais" et gaz recirculé (mais surtout valable à la cathode il semblerait, donc ne me concerne pas).

Quelques bonnes infos générales sur l'H2.

Article directement utilisé par Ling Xu pour construire son modèle d'auxiliaires.

Il est bien écrit et est un bon modèle pour faire un article.

Il y a quelques valeurs pour les coefficients des orifices des collecteurs.

Des données supplémentaires sur les purges.

Des données sur la condensation de l'eau lors du mélange entre gaz "frais" et gaz recirculé (mais surtout valable à la cathode il semblerait, donc ne me concerne pas).

- Quelques bonnes infos générales sur l'H2. doi:10.1016/j.ijhydene.2019.11.150.

[24] L. Xu, Z. Hu, C. Fang, L. Xu, J. Li, M. Ouyang, A reduced-dimension dynamic model of a proton-exchange membrane fuel cell, *Intl J of Energy Research* 45 (12) (2021) 18002–18017, article principal sur lequel je me base pour travailler sur ma thèse.
Il vient d'une équipe avec laquelle Zhongliang est en lien. doi:10.1002/er.6945.

[25] F. Van Der Linden, E. Pahon, S. Morando, D. Bouquain, Proton-exchange membrane fuel cell ionomer hydration model using finite volume method, *International Journal of Hydrogen Energy* 47 (51) (2022) 21803–21816, cet article de Fabian donne un modèle 1D de la MEA. Il se concentre particulièrement sur la membrane.
Il considère une membrane qui peut se dilater, contrairement à la plupart des travaux.
Modèle 1D de Fabian portant uniquement sur la MEA. Le modèle est quand même poussé, en dynamique. doi:10.1016/j.ijhydene.2022.05.012.

[26] R. Gass, Z. Li, R. Outbib, S. Jemei, D. Hissel, A Critical Review of Proton Exchange Membrane Fuel Cells Matter Transports and Voltage Polarisation for Modelling, *Journal of The Electrochemical Society* (2024). doi:10.1149/1945-7111/ad305a.

[27] J. Wang, H. Jiang, G. Chen, H. Wang, L. Lu, J. Liu, L. Xing, Integration of multi-physics and machine learning-based surrogate modelling approaches for multi-objective optimization of deformed GDL of PEM fuel cells, *Energy and AI* 14 (2023) 100261, articles faisant le lien entre modèles physiques et modèles d'IA. doi:10.1016/j.egyai.2023.100261.

[28] B. Wang, Z. Yang, M. Ji, J. Shan, M. Ni, Z. Hou, J. Cai, X. Gu, X. Yuan, Z. Gong, Q. Du, Y. Yin, K. Jiao, Long short-term memory deep learning model for predicting the dynamic performance of automotive PEMFC system, *Energy and AI* 14 (2023) 100278, articles faisant le lien entre modèles physiques et modèles d'IA. doi:10.1016/j.egyai.2023.100278.

[29] G. E. Karniadakis, I. G. Kevrekidis, L. Lu, P. Perdikaris, S. Wang, L. Yang, Physics-informed machine learning, *Nat Rev Phys* 3 (6) (2021) 422–440, document donné par Zhongliang afin d'apprendre des techniques de Machine Learning implémentant directement dans l'apprentissage les modèles physiques plutôt que se baser uniquement sur une base de donnée déjà établie. doi:10.1038/s42254-021-00314-5.

[30] SciPy, *Scipy.Integrate.Solve_ivp* (2024).

[31] K. Jiao, X. Li, Water transport in polymer electrolyte membrane fuel cells, *Progress in Energy and Combustion Science* 37 (3) (2011) 221–291, source principale de l'article 2016 de Ling Xu. C'est un document très complet et très bien réalisé.
Je l'ai précédemment utilisé pour la gestion de l'eau, mais il semble que la thermique est aussi étudiée. doi:10.1016/j.pecs.2010.06.002.

[32] S. Ge, X. Li, B. Yi, I.-M. Hsing, Absorption, Desorption, and Transport of Water in Polymer Electrolyte Membranes for Fuel Cells, *J. Electrochem. Soc.* 152 (6) (2005) A1149, article important permettant d'obtenir les constantes de temps associées aux flux entre membrane et catalyseur.
C'est l'article originel et c'est le seul qui a fait des expériences aussi poussées sur le sujet. doi:10.1149/1.1899263.

[33] A. H.-D. Cheng, D. T. Cheng, Heritage and Early History of the Boundary Element Method, *Engineering Analysis with Boundary Elements* 29 (3) (2005) 268–302. doi:10.1016/j.enganabound.2004.12.001.

[34] A. Z. Weber, J. Newman, Transport in Polymer-Electrolyte Membranes, *Journal of The Electrochemical Society* (2004).

[35] A. Dicks, D. A. J. Rand, *Fuel Cell Systems Explained*, third edition Edition, Wiley, Hoboken, NJ, 2018.

[36] R. P. O'Hare, S.-W. Cha, W. G. Colella, F. B. Prinz (Eds.), *Fuel Cell Fundamentals*, third edition Edition, John Wiley & Sons Inc, Hoboken, New Jersey, 2016.

[37] Z. Yang, Q. Du, Z. Jia, C. Yang, K. Jiao, Effects of operating conditions on water and heat management by a transient multi-dimensional PEMFC system model, *Energy* 183 (2019) 462–476, référence 21 de Ling Xu. Jiao K. est l'un des co-auteurs.
Cet article semble très bien fait et me permet entre autre de bien reconsiderer le calcul de la tension de la pile: "concentration loss" + Nernst potentiel qui se place au niveau du CL et pas à la frontière avec le GC.
Il propose aussi une bonne modélisation des auxiliaires: They studied the effects of BOP operating parameters on the water and temperature distributions of fuel cells with a pseudo-two-dimensional fuel cell model combined with a BOP model.
Il donne des informations sur les équations de la MPL et ses paramètres. doi:10.1016/j.energy.2019.06.148.

[38] M. Santarelli, M. Torchio, P. Cochis, Parameters estimation of a PEM fuel cell polarization curve and analysis of their behavior with temperature, *Journal of Power Sources* 159 (2) (2006) 824–835, article donnant des informations sur la réalisation expérimentale d'une courbe de polarisation. doi:10.1016/j.jpowsour.2005.11.099.

[39] M. V. Williams, H. R. Kunz, J. M. Fenton, Analysis of Polarization Curves to Evaluate Polarization Sources in Hydrogen/Air PEM Fuel Cells, *Journal of The Electrochemical Society* 152 (3) (2005) A635. doi:10.1149/1.1860034.

[40] R. Gass, Z. Li, R. Outbib, S. Jemei, D. Hissel, AlphaPEM: An open-source dynamic 1D physics-based PEM fuel cell model for embedded applications, *SoftwareX* 29 (2025) 102002. doi:10.1016/j.softx.2024.102002.

[41] H. Meng, A Two-Phase Non-Isothermal Mixed-Domain PEM Fuel Cell Model and Its Application to Two-Dimensional Simulations, *Journal of Power Sources* 168 (1) (2007) 218–228. doi:10.1016/j.jpowsour.2007.03.012.

[42] B. Xie, M. Ni, G. Zhang, X. Sheng, H. Tang, Y. Xu, G. Zhai, K. Jiao, Validation methodology for PEM fuel cell three-dimensional simulation, *International Journal of Heat and Mass Transfer* 189 (2022) 122705, article conseillé par mon reviewer 2 de mon article review pour discuter d'une autre manière de modéliser les flux d'eau liquide dans la pile. doi:10.1016/j.ijheatmasstransfer.2022.122705.